Active dynamics of microtubule and motor protein networks

Active dynamics of microtubule and motor protein networks

A DISSERTATION PRESENTED
BY
PETER J. FOSTER
TO
THE JOHN A. PAULSON SCHOOL OF ENGINEERING AND APPLIED SCIENCES

IN PARTIAL FULFILLMENT OF THE REQUIREMENTS
FOR THE DEGREE OF
DOCTOR OF PHILOSOPHY
IN THE SUBJECT OF
APPLIED PHYSICS

HARVARD UNIVERSITY
CAMBRIDGE, MASSACHUSETTS
APRIL 2017

Dissertation Advisor: Professor Daniel J. Needleman Peter J. Foster

Active dynamics of microtubule and motor protein networks

Abstract

Cellular components have the remarkable ability to self-organize in space and time into higher order structures necessary to carry out biological functions. One example of such a structure is the spindle apparatus, a subcellular organelle composed primarily of microtubules that segregates chromosomes during cell division and ensures that each of the resulting daughter cells receives a complete copy of the genetic material. These microtubules are organized in part by molecular motor proteins that can crosslink and exert forces on microtubules using energy from ATP hydrolysis. Much is known about how individual motor proteins slide pairs of microtubules, but how motor proteins organize large collections of filaments, such as one finds in the spindle, remains unclear. How can length scales be bridged such that large length scale behaviors of the microtubule network can be understood in terms of nanometer scale motor-protein interactions?

Chapter 1 provides a brief overview on two motor proteins important for spindle assembly, the role of these motor proteins during spindle self-organization, and the organization of microtubule networks more generally. Chapter 2 presents quantitative results demonstrating the active contraction of millimeter scale microtubule networks in *Xenopus* oocyte extracts. An active fluid model is proposed that can quantitatively explain the dynamics and internal architecture of these contracting networks, as well as how these properties vary under perturbations to sample geometry and motor concentration. Chapter 3 extends these results and provides further tests of this model by providing quantitative measurements of the effects of varying microtubule length and density on the dynamics of these networks. Chapter 4 presents a reconstitution of this bulk network contraction in a system composed of purified dynein and microtubules. Chapter 5 presents results on networks composed of purified microtubules and the motor protein XCTK2, which undergo a spontaneous bulk contraction followed by bulk extension of the network. Chapter 6 presents a summary of the conclusions of the thesis as a whole. Finally, the appendices contain a derivation of the active fluid model, Material and Methods for the thesis as a whole, and an additional chapter detailing the development and testing of a Bayesian approach to FLIM data analysis.

Contents

Author List

The following authors contributed to Chapter 1:

Daniel J. Needleman.

The following authors contributed to Chapter 2:

Sebastian Fürthauer, Michael J. Shelley and Daniel J. Needleman.

The following authors contributed to Chapter 3:

Sebastian Fürthauer, Michael J. Shelley and Daniel J. Needleman.

The following people contributed to Chapter 4:

Ruensern Tan, Richard McKenney and Daniel J. Needleman.

The following people contributed to Chapter 5:

Che-Hang Yu and Daniel J. Needleman.

The following authors contributed to Appendix A:

Bryan Kaye, Tae Yeon Yoo, and Daniel J. Needleman.

The following authors contributed to Appendix B:

Sebastian Fürthauer, Michael J. Shelley and Daniel J. Needleman.

Listing of figures

In memory of Fr. Ray Foster.

Acknowledgments

I'd like to thank Sebastian Fürthauer and Michael Shelley for an excellent and productive collaboration, and Ruensern Tan, Rick McKenney, Thomas Surrey, Tim Mitchison, Stephanie Ems-McClung, and Claire Walczak for providing materials. Thanks to all of the members of the Needleman lab for all of their help, guidance, and support. I'd especially like to thank Bryan Kaye for teaching me so much and for always being there for me. You've truly been a great friend. I'd also like to thank Bryan Hassell for the help and encouragement throughout the years. My time in graduate school was much better for having you in it. I'd like to thank Dan Needleman for being such an excellent advisor. You taught me what it means to do good science. I'd like to thank my parents, Jim and Susie Foster, for all of their love and support and for always believing in me. Finally, I'd like to thank Julia Schwartzman for all of the love, help, support, and crazy ideas.

1

Introduction

1.1 INTRODUCTION

Many cellular structures are composed of microtubules; from the branching networks found in neurons, to spindles formed during cell division, to asters found in interphase cells. These structures not only contain microtubules, but also a variety of other proteins that influence how the microtubules interact and behave. How do the properties of these structures arise from the behaviors of their constituent molecules? Answering this question would provide fundamental insight into cell biology and would allow an understanding of how changes influencing the constituent molecules impact the properties of the structure as a whole. This would also shed light on how evolutionary changes to constituent proteins influence and are influenced by the properties of the cellular-scale structures. This question has yet to be fully answered for any microtubule based structure.

The spindle is the microtubule-based structure that segregates chromosomes during cell division. Motor proteins, which use chemical energy derived from ATP hydrolysis to move on microtubules, are one of the primary determinants of spindle structure and are required for proper chromosome segregation. There are a variety of different motor proteins, whose relative importance varies between spindles in different systems. In *Xenopus* egg extracts, one of the most well studied model systems for investigating spindle assembly, two of the most important motor proteins for proper spindle assembly are dynein and Kinesin-5[1]. Inhibiting either of these proteins leads to gross morphological changes in spindle architecture, transitioning spindles from their ordinarily fusiform shape to ”barrels” with unfocused poles for dynein inhibition[2] or astral monopoles for Kinesin-5 inhibition[3]. Intriguingly, when dynein and Kinesin-5 are simultaneously inhibited, spindles have the same gross morphology as unperturbed spindles[4]. It remains unclear why these changes in morphology result from the loss of dynein and Kinesin-5 activity.

Different ideas have been proposed to explain the effect of these motor proteins on the structure and dynamics of the spindle. In *Xenopus* spindles, dynein has been proposed to transport a variety of proteins to the poles, including NuMA[5], microtubule disassembly factors[6], and Kinesin-5[7]. After being transported by dynein, the activities of these proteins may lead to the focusing of microtubules at the poles. Kinesin-5 has been proposed to promote microtubule depolymerization in budding yeast[8] and to be a microtubule polymerase[9]. Other models have suggested that dynein and Kinesin-5 function by crosslinking, sliding, and transporting microtubules within the spindle[10,11,12]. In the case of dynein, it's unclear whether the primary cargo is microtubules or other proteins. In the case of Kinesin-5, it's unclear whether its dominant contribution is microtubule sliding or the regulation of polymerization dynamics.

How can one understand the emergence of spindle dynamics and morphology from the properties of dynein and Kinesin-5? Here, we propose extrapolating from the molecular behaviors of the motor proteins to the effective interactions between microtubules, and from these effective interactions to the behaviors of collections of motors and microtubules, such as the spindle. Extensive work has been done focusing on these different length scales. We now know many details of how motors interact with individual microtubules, how motors cause pairs of microtubules to interact, and how collections of motors and microtubules organize, but connecting these length scales remains a challenge. Bridging these length scales would allow quantitative predictions of how spindle dynamics and morphology arise from the molecular properties of the spindle's constituent components.

1.2 Motor Interactions with Individual Microtubules

To begin to understand how these motors function in the spindle, one fruitful approach has been to study the interactions of motor proteins with individual microtubules in purified systems. In what ways can a motor protein interact with a microtubule? Motor proteins can bind a microtubule, walk on the microtubule, and unbind (Figure 1.1A). Even from these simple interactions, surprising complexity can emerge which is only partially understood. This complexity is further complicated by additional layers of biochemical regulation.

Structural differences between dynein and Kinesin-5 lead to differences in how they bind microtubules. Kinesin-5 is a homotetramer, with each subunit containing a mo-

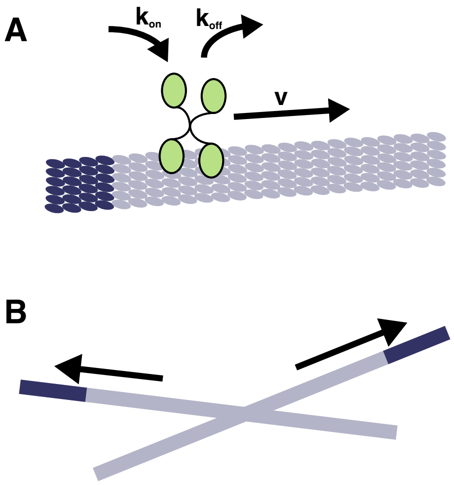

Figure 1.1: (A) Motor proteins walk along microtubules with a characteristic directionality. Motors can bind to a microtubule at rate k_{on}, and fall off of a microtubule at rate k_{off}. (B) Motor proteins cause microtubules to interact and can cause relative sliding between the filaments.

tor domain[13,14]. This allows Kinesin-5 to simultaneously bind two microtubules and walk on both[15]. Microtubule binding by Kinesin-5 is cell cycle regulated in *Xenopus* egg extracts by Cdk1 phosphorylation[16]. Dynein contains only two motor domains. Dynein is capable of crosslinking microtubules through an additional microtubule binding domain in another protein in the dynein complex[1,17]. One possible candidate is NuMA, which contains a microtubule binding domain[18], and has been proposed be involved in microtubule crosslinking[5]. This allows dynein to walk on one microtubule while passively binding another, though other modes have been suggested, such as the simultaneous binding of each motor domain to a separate microtubule[19].

For both dynein and Kinesin-5, an extensive amount is known about how they bind and hydrolyze ATP and about the structural details of how the motors step.[20,21]. Dynein is a minus end directed motor protein. While yeast dynein is processive on its own[22], mammalian dynein processivity is regulated by activating proteins, such as

BicD2[23] and Hook proteins[24]. Lis1 also influences dynein processivity by decreasing dynein's velocity and increasing its association time with microtubules[25]. Kinesin-5 is a plus end directed motor protein with two distinct modes of motion on individual microtubules; a constant velocity mode with directed motion, and a diffusive mode showing no directional bias[26]. The relative importance of these two modes of motion within spindles is unclear. Kinesin-5 processivity on individual microtubules depends strongly on ionic strength, with Kinesin-5 motion being largely diffusive rather than directional at close to physiological ionic strength[27].

The motor unbinding rate can in principle vary spatially along microtubules, leading to an inhomogeneous spatial distribution of motor density. Motors could concentrate on microtubule ends through a variety of different mechanisms, such as having a smaller off rate at the microtubule end. This could lead to a molecular ”traffic jam”, as demonstrated for Kinesin-8[28]. In *Xenopus* extracts, dynein buildup on minus ends has been proposed to play a direct role in aster formation[29] and bulk network contraction[30] and this minus end buildup of dynein can be visualized in purified systems[23]. Dynein buildup on minus ends has also been reported in spindles[31,32], where it has been proposed to play a role in kinetochore fiber positioning. Like dynein, Kinesin-14 has also been shown to accumulate on microtubule minus ends in a purified system[33]. Intriguingly, dynein can also be targeted to dynamic microtubule plus ends[34], and this targeting has been recapitulated in a purified system[35]. While the importance of the plus end targeting of dynein for spindle assembly is unclear, it has been proposed to play a role in spindle positioning in some systems[36]. Kinesin-5 can localize to microtubule plus ends *in vitro*[9,15], though it is unclear if Kinesin-5 localizes to microtubule plus ends *in vivo*, and if so what the mechanical consequences of this localization would be.

From these three conceptually simple interactions between a motor protein and a microtubule, surprisingly complex behaviors can emerge that are only partially understood. While much is known about how dynein and Kinesin-5 interact with microtubules, further work is needed to fully understand these interactions and their regulation, both *in vitro* and *in vivo*.

1.3 MOTOR INTERACTIONS WITH MICROTUBULE PAIRS

How can the molecular behaviors of motor proteins be connected with the organization of the spindle? One approach is to directly study how motors mediate interactions between microtubules (Figure 1.1B). Studying the problem at this scale provides a convenient intermediate-length scale that allows connections to be made to both the molecular properties of the motors and the large-scale collective organization of the spindle. The simplest of these interactions are the pairwise interactions between two microtubules. There has been a significant amount of theoretical work employing multiple strategies to coarse grain over these pairwise microtubule interactions to describe the emergent properties of collections of filaments and motors[30,37,38,39,40,41], though the extent to which these simplified models can quantitatively bridge these two scales remains to be seen, particularly for *in vivo* systems.

What would one want to know to fully characterize pairwise interactions between microtubules? Different theoretical approaches are based on different models of the pairwise interactions themselves. For example, some approaches model microtubule interactions as collision events, explicitly taking into account only the initial and final microtubule positions and relative angles while remaining agnostic about the details of the interaction[39]. Other approaches include motor activity by assuming a constant sliding velocity between interacting filaments[37]. Here, we define pairwise microtubule interactions to be the relative velocity distributions of two sliding filaments. This definition has the advantage of being general enough to encompass a variety of different sliding behaviors, while being specific enough that it can in principle be measured. The velocity distributions can potentially depend on many things, including the relative angle between the microtubules[42], which in part arise from the polarity preferences of the motor protein, and weak frictional forces generated between the microtubules themselves, recently characterized in a purified system[43,44]. The relative position of the microtubules can influence their interaction, as some motor proteins have been proposed to build up on filament ends, leading to locally differing interactions[30,45,46,42]. Finally, external forces on the microtubules can change their effective interactions through the force-velocity relationship of the motor protein[47].

Some work has been done beginning to characterize pairwise microtubule interactions in purified systems containing stabilized microtubules and a single kind of motor. These studies have thus far focused on measuring the velocity distributions only for aligned sliding microtubules. Kinesin-5 has been shown to cause antiparallel microtubules to slide relative to each other, to cause microtubules to co-align, and to statically crosslink parallel microtubules[7,15,47]. Similar work using purified dynein has also shown that it causes antiparallel microtubule sliding and co-alignment[19], though the dynein construct in this case may not be representative of the dynein complex found in spindles due to the exclusion of dynein adaptor proteins such as BicD2[23]. Further work is needed exploring how these velocity distributions vary with the relative angle and position of the microtubules as well as how these velocity distributions are influenced by other regulatory proteins, particularly for dynein.

While no explicit measurements exist of the angular dependence of the relative velocity distributions for sliding microtubules, evidence suggests there may be an effect.

Kinesin-5 has been shown to have an ≈3 fold binding preference for antiparallel microtubules versus parallel microtubules[48], and both dynein and Kinesin-5 have been proposed to display a preference for sliding antiparallel microtubules[15,19]. These preferences could arise in part from the motor's torsional elasticity, i.e. how hard it is for a motor protein bound to a microtubule to rotate such that it can bind in a given conformation to a second microtubule. While the torsional elasticity has been measured for Kinesin-1 constructs[49,50,51] and found to be quite low, detailed measurements for dynein and Kinesin-5 are lacking. Indirect evidence suggests that Kinesin-5's torsional elasticity is also relatively low[15]. In addition to an angular dependence stemming from the molecular properties of the motor protein, the angle between microtubules sets the overlap length of the microtubules and hence how many motors can simultaneously bind to the microtubule pair[47]. Further understanding how these motor proteins interact with microtubules as a function of the relative microtubule angle will inform the role of these proteins in spindles.

Some work has also been done characterizing Kinesin-14, a minus end directed member of the Kinesin family crucial for proper spindle assembly in Drosophila[52] and thought to serve the same functional role as dynein in some systems[53]. Kinesin-14 was found to robustly slide microtubules when they are antiparallel[33,54]. Intriguingly, Kinesin-14 can also slide parallel microtubules, but only in short bursts that exponentially slowed[33]. When the minus ends of antiparallel sliding microtubules met, the sliding microtubule was found to be able to swivel around until it reached a parallel configuration where it became statically linked[33]. This argues that Kinesin-14 may not simply fall off upon reaching the microtubule minus end and instead may building up in a ”traffic jam”, as has been shown for Kinesin-8[28]. Kinesin-14 can also form microtubule asters in purified systems,[54], consistent with predictions that aster formation happens in part due to motor buildup on filament ends[29,30]. While dynein has been suggested to localize to minus ends in cells and cell extracts[29,30,32], to what extent Kinesin-5 localizes to plus ends remains to be seen.

While some experimental work has been done in this area, many open questions remain. To what extent do motor proteins in the spindle compete or cooperate? Some work has been done considering the issue of motor competition for Kinesin-5 and Kinesin-14 in a purified system[54], but within spindles we don't know how many motors proteins are bound to a given pair of microtubules, and thus we don't know if this is even a relevant question. While experiments using purified components can give insight into their behaviors, how well can one extrapolate from *in vitro* behaviors to *in vivo* functions? To what extent can one extrapolate from pairwise microtubule interactions to collective behaviors? While for many physical systems, a knowledge of pairwise interactions is sufficient to quantitatively predict collective effects, it has been argued that this is insufficient for motor induced sliding in motility assays[55]. To what extent this is the case for motor proteins in the spindle remains to be seen. Further work is needed quantitatively measuring pairwise microtubule interactions, particularly in complex environments mimicking the cell, and connecting these measurements with properties of the spindle.

1.4 Collective Behavior of Motor Proteins and Microtubules

Another approach is to directly investigate the large-scale properties of collections of microtubules and motors. Directly investigating collective properties can shed light on emergent, collective behaviors that may be non-obvious from either the molecular properties of the motor protein or from the pairwise microtubule interactions mediated by the motor protein. The spindle is itself a collection of microtubules, and thus

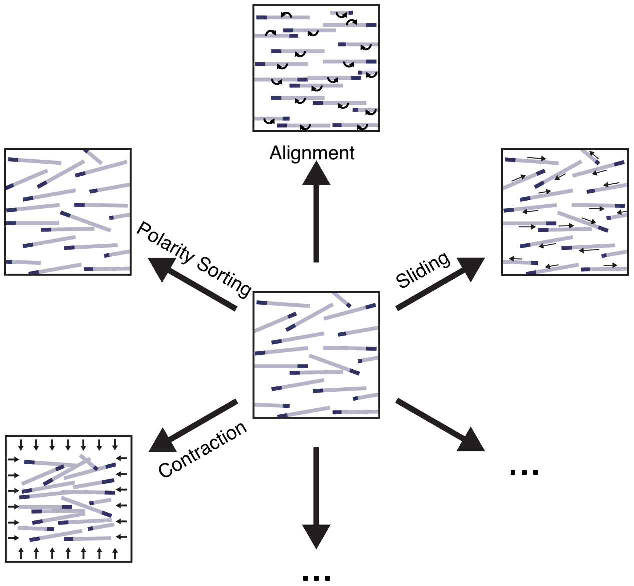

Figure 1.2: Motor induced interactions between microtubules can cause a variety of collective behaviors, including sliding, alignment, polarity sorting, bulk contraction and many others.

studying the collective behaviors of motors proteins and microtubules can inform how dynein and Kinesin-5 lead to collective behaviors within the spindle.

What are the ways in which motor proteins can organize collections of microtubules? Imagine a small region of a microtubule network (Figure 1.2, center). These microtubules could potentially be organized by motors in many different ways (Figure 1.2). They could generate contractile stresses that cause the microtubules to compact. They could reorient the microtubules, pointing them in the same direction, which could be done in a matter that reflects the polarity of the microtubules. They could slide the microtubules relative to each other, possibly without a net change in the density, alignment, or overall polarity in the network. These are only a few possibilities of the many ways the motors can drive the organization of microtubule collections, and many of these possibilities are not mutually exclusive. The theory of active matter provides a mathematical formalism to enumerate the ways networks of microtubules and motors can rearrange and enables calculations of their corresponding behaviors[40,56]. The parameters of an active matter theory determine the extent to which different rearrangements occur spontaneously, how difficult they are to induce, and how they are coupled. Active matter theories make a variety of general predictions which are independent of the precise value of their parameters, including the generic instability of large, oriented arrays of microtubules and motors[57] which, it is tempting to speculate, could be the cause of the apparent upper limit to spindle size[58,59]. Active matter theories can predict the detailed behaviors of systems of interest, but in order to do so, the numerical values of the theory's parameters are required, which must be measured experimentally[30,60], or, possibly, derived from behaviors of the system's components[61].

Very general arguments suggest that active matter theories should provide an accurate description of sufficiently large collections of microtubules and motors, but for many systems, their applicability is yet to be experimentally tested. Thus, there are two questions for any particular system: 1) to what extent are its behaviors well captured by active matter theories and 2) if they are, what are the parameter values corresponding to the system? Answering these questions requires a close interplay between experiment and theory. It has recently been shown that the internal dynamics and morphology of *Xenopus* egg extract spindles are quantitatively described by a suitably constructed active matter theory, which allowed nearly all of the parameters of the theory to be measured[60]. This work provides a quantitative framework for understanding spindle structure and behavior, and highlights the key physical processes occurring in the spindle, such as the continued co-alignment of spindle microtubules[60]. Establishing the contribution of different motor proteins in the spindle requires understanding their collective behavior with microtubules. Microtubules assembled outside the spindle in *Xenopus* egg extracts form a network that contracts in a manner that can be quantitatively described by a simple active matter theory[30]. This contraction is predominantly driven by dynein, suggesting that dynein generates isotropic contractile stresses in the spindle[30]. Reconstituted networks of purified Kinesin-14 and microtubules can also exhibit contractions[45,54]. The relative roles of these motors could be clarified by determining the extent to which Kinesin-14-driven contractions are similar or different from dynein-driven contractions, which have not yet been investigated in purified systems. Mixtures of microtubules and other motors can produce extensile networks with a tendency for microtubules to co-align[62,63], which behave in a manner qualitative consistent with predictions from active matter theories[41,64]. Unlike other motor proteins studied, purified *Xenopus* Kinesin-5 was shown to be unable to organize large-scale structure in a microtubule network, instead causing only large-scale density fluctuations[54]. This argues that, unlike dynein, Kinesin-5 may be unable to exert a net stress in *Xenopus* spindles.

How might dynein and Kinesin-5 enter into active matter theories? Microtubule crosslinking by motor proteins tends to align microtubules locally, which contributes to an effective elasticity that penalizes deformations in the microtubule network. Motors also contribute through the generation of active stresses, which can take one of two forms. The stresses can be isotropic, causing the density of the network to either decrease (extensile, Figure 1.3A) or increase (contractile, Figure 1.3B). Active stresses can also be dipolar, with the total density being conserved. Dipolar stresses are defined relative to the orientation of the microtubule bundle and can be extensile (Figure 1.3C) if the motor proteins generate flows that push material away along the axis of the microtubule bundles, or contractile (Figure 1.3D) if the flows pull material

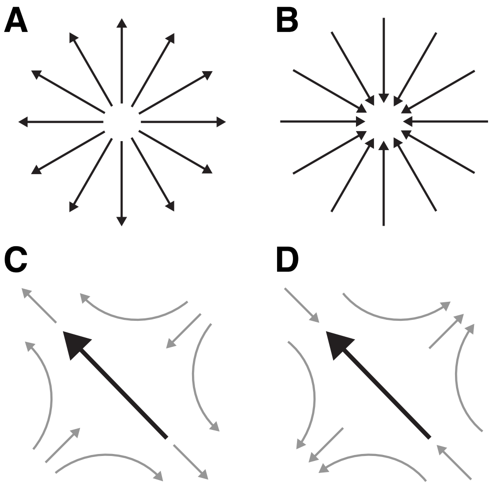

Figure 1.3: A variety of active stresses are possible, including (A) isotropic extensile stress, (B) isotropic contractile stress, (C) dipolar extensile stress, and (D) dipolar contractile stress. Arrows in (A) and (B) represent local stresses. In (C) and (D), black arrows represent the orientation of the microtubule bundle, while gray arrows represent material flows.

in along the axis of the microtubule bundle.

Active matter theories provide a mathematical framework to understand the large-scale organization and behaviors of collections of microtubules and motor proteins. While these theories have been successful in describing behaviors in *Xenopus* egg extracts[60], how applicable they are to spindles in other systems remains to be tested. Active matter theories provide a natural language for describing the large-scale properties of the system, and in some cases, the connection has been made between these large-scale properties and the behaviors of the network's constitutive motor proteins[30].

1.5 Conclusions

Taken together, this suggests a tentative model for the roles of dynein and Kinesin-5 in the spindle (Figure 1.4). Dynein accumulates on microtubule minus ends[31,23,32],

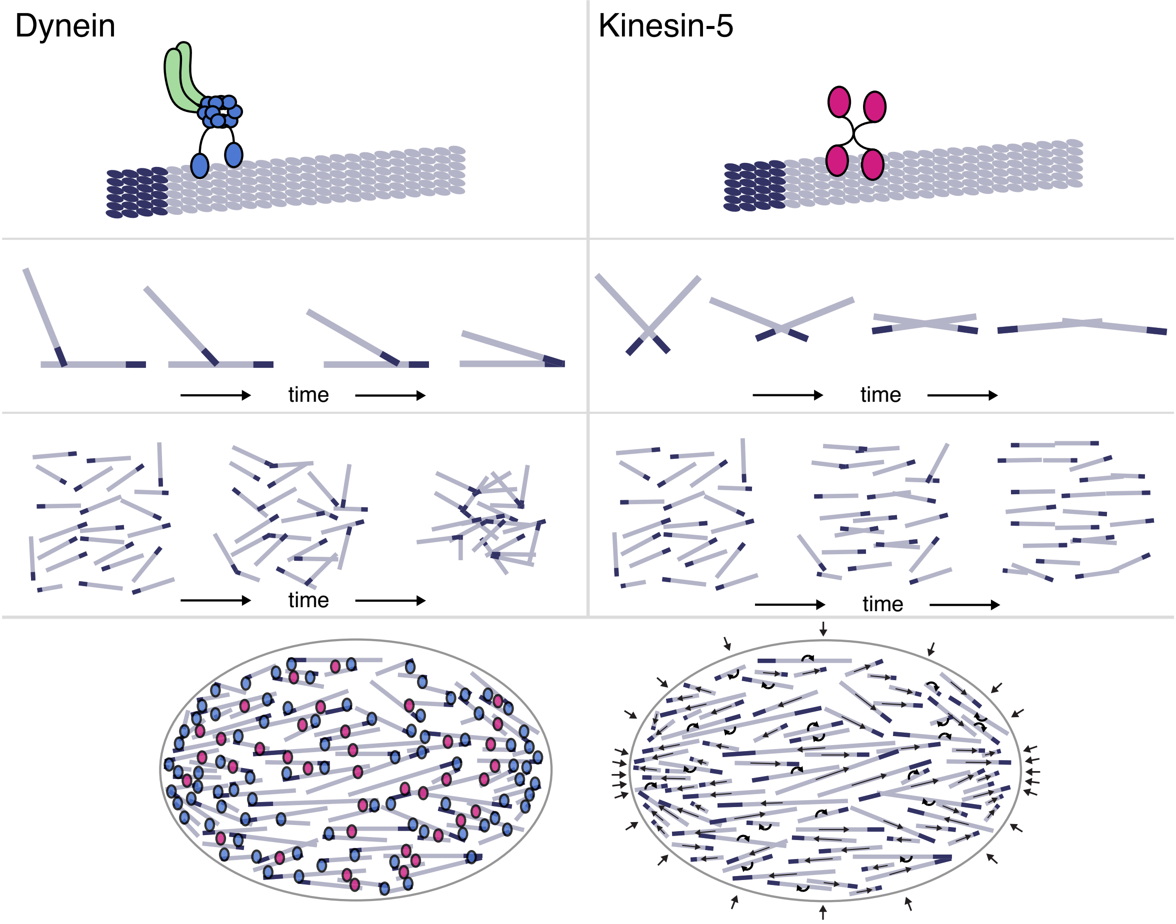

Figure 1.4: Possible roles for dynein and Kinesin-5 in pairwise microtubule interactions and their resulting collective behaviors. Dynein slides microtubules leading to clustering of their minus ends. This effect leads to a bulk contraction in collections of filaments. Kinesin-5 slides, orients, and polarity sorts pairs of microtubule filaments. This leads to local polarity sorting and a global alignment of microtubules. In spindles, both motors are present, and both of these effects are happening simultaneously.

where it can slide microtubules, leading to a clustering of the minus ends. This minus end clustering gives rise to an isotropic contractile stress[45,30], which in turn leads to spindle pole formation. This model for dynein naturally explains previous observations that were difficult to explain, such as the dynein dependence of spindle fusion[1], and the greater cohesion of microtubules at spindle poles[65], where dynein normally accumulates. Kinesin-5 crosslinks microtubules while walking toward their plus ends, causing microtubules to co-orient and antiparallel microtubules to slide apart. This behavior leads to microtubule alignment, sliding, and polarity sorting, but does not contribute to the active stress. This behavior also gives rise to mass transport towards the spindle poles[66], the profile of microtubule polarity throughout the spindle[67], and, together with the active stress generated by dynein, the overall bipolar nature of spindles[60]. These activities of dynein and Kinesin-5 could be occurring simultaneously throughout the spindle, and argues that they do not directly compete against each other.

While this proposed model is consistent with experimental observations, it comes with several caveats. Most aspects of the model are uncertain, and further work carried out directly in spindles will be required to investigate the model's implications. This model only considers the mechanical aspects of these motors but does not directly consider other proposed roles for these proteins which could be important aspects of spindle formation. Furthermore, this model does not include the possible spatial regulation of the motor's activities, which again could have implications for spindle organization and stability.

Dynein and Kinesin-5 have been shown to be crucial for the proper organization of the spindle in *Xenopus* egg extracts, but their relative importance is diminished in other organisms and in some organisms they are absent altogether[68,69]. This raises the question of if, rather than the molecular details of the system, the higher level attributes are the same in spindles across organisms, possibly due to the contributions of other motor proteins. If not, how do different higher level attributes lead to spindles that can perform the same basic function? If it is the case that higher order attributes are the same in spindles across organisms, we think it is an intriguing possibility that it is in fact these attributes that evolution is selecting for, rather than the detailed behavior of the individual proteins. Much more work is needed to distinguish these possibilities.

This chapter details and largely reproduces work previously published as, PJ Foster, S Fürthauer, MJ Shelley, DJ Needleman, "Active contraction of microtubule networks", eLife 2015;10.7554/eLife.10837 .

2

Active contraction of microtubule networks

2.1 Introduction

Here, we investigate the motor-driven self-organization of stabilized microtubules in *Xenopus* meiotic egg extracts. These extracts are nearly undiluted cytoplasm and recapitulate a range of cell biological processes, including spindle assembly and chromosome segregation[41]. We have discovered that, in addition to microtubules forming asters in this system as previously reported[29], the asters assemble themselves into a macroscopic network that undergoes a bulk contraction. We quantitatively characterized these contractions and found that their detailed behavior can be well understood using a simple coarse-grained model of a microtubule network in which dynein drives the clustering of microtubule minus ends. This end clustering mechanism leads to a novel form of active stress, which drives the system to a preferred microtubule density. Our results suggest that the dynein-driven clustering of microtubule minus ends causes both aster formation and network contraction, and have strong implications for understanding the role of dynein in spindle assembly and pole formation. Furthermore, the close agreement we find between experiments and theory demonstrates that simple continuum models can accurately describe the behavior of the cytoskeleton, even in complex biological systems.

2.2 Results

To further study the motor-induced organization of microtubules, we added 2.5 μM Taxol to *Xenopus* egg extracts and loaded them into microfluidic channels (Fig 2.1 A). Taxol causes microtubules to rapidly assemble and stabilize[70], which allowed us to decouple the effects of motor-driven self-assembly from the complicating effects of polymerization-depolymerization dynamics. In some regions of the channel, microtubules organized into asters (Fig 2.1 B) as observed previously[29]. A NUMA antibody was used to locate microtubule minus ends[70], and was found to localize to the aster core, confirming the polarity of the aster[71]. Isolated asters were found to interact and coalesce (Fig 2.1 C). In other regions of the channel, microtubules formed networks of aster-like structures (Fig 2.1 D), which were highly dynamic and exhibited large scale motion that persisted for several tens of seconds (Fig 2.1 E). NUMA was found to localize to the interior of these structures, confirming their aster-like na-

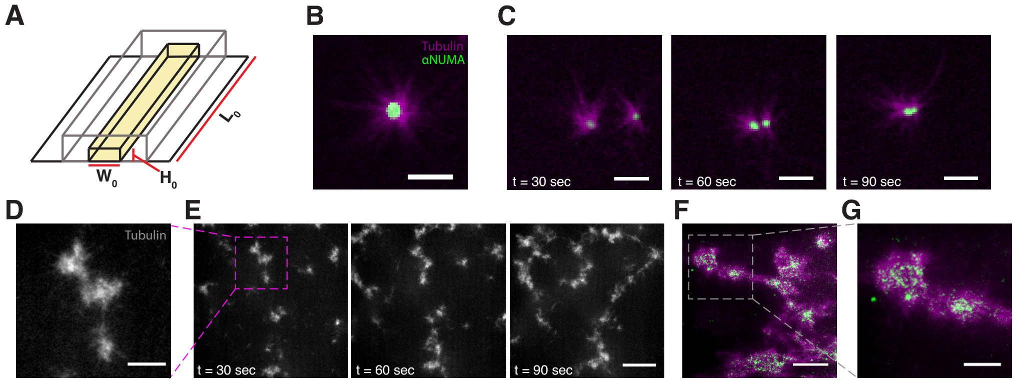

Figure 2.1: Stabilized microtubules form asters in *Xenopus* egg extracts. (A) Experiments were performed in thin rectangular channels of width W_0, height H_0 and length L_0. (B) In some regions of the channel, microtubules organize into asters, with minus ends localized in the aster core (Scale bar, 5μm). (C) Isolated asters fuse together over minute timescales (Scale bar, 5μm). (D) Aster-like structures form in other regions of the channel (Scale bar, 10μm) (E) Aster-like structures show large scale movement on minute timescales. (Scale bar, 25μm). (F) NUMA localizes to the network interior (Scale bar, 20μm). (F) Closeup of aster-like structure showing NUMA localized on the interior (Scale bar, 10μm).

ture (Fig 2.1 F, G).

To characterize these large scale motions, we next imaged networks at lower magnification, obtaining a field of view spanning the entire channel width. The networks, which initially filled the entire channel (width $W_0 = 1.4$mm), underwent a strong contraction, which was uniform along the length of the channel (Fig 2.2 A). The contractile behavior of these microtubule networks is highly reminiscent of the contractions of actin networks in these extracts[72], but in our experiments actin filaments are not present due to the addition of 10 $\frac{\mu g}{mL}$ Cytochalasin D. We characterized the dynamics of microtubule network contractions by measuring the width , W(t) , of the network as a function of time (Fig 2.2 B). Occasionally we observed networks tearing along their length, yet these tears seemed to have little impact on the contraction dynamics far from the tearing site, arguing that the Poisson ratio of the network is ≈ 0. We

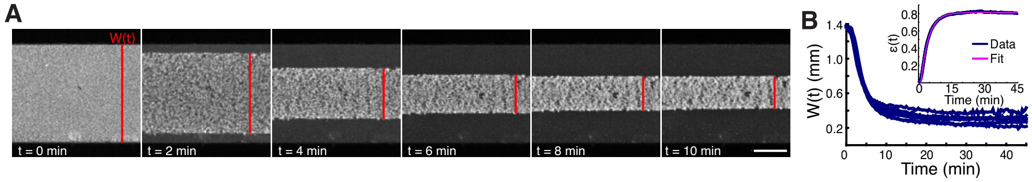

Figure 2.2: Stabilized microtubules form a contractile network in *Xenopus* egg extracts. (A) Low magnification imaging shows that microtubules form a contractile network (Scale bar, 500μm). (B) The width of the microtubule network decreases with time (n = 6 experiments). (Inset) Representative plot of ϵ(t) (Blue line) and fit from Eqn 2.1 (Pink line), with $\epsilon_\infty = 0.81$, $\tau = 3.49$ min, $T_c = 1.06$ min.

then calculated the fraction contracted of the network:

$$\epsilon(t) = \frac{W_0 - W(t)}{W_0}, \tag{2.1}$$

The time course of ϵ(t) was found to be well fit by an exponential relaxation:

$$\epsilon(t) \simeq \epsilon_\infty[1 - e^{\frac{-(t-T_c)}{\tau}}], \tag{2.2}$$

where ϵ_∞ is the final fraction contracted, τ is the characteristic time of contraction, and T_c is a lag time before contraction begins (Fig 2.2 B, Figure 2.3).

We next sought to investigate which processes determine the time scale of contraction and the extent that the network contracts. For this, we exploited the fact that different mechanisms predict different dependence of the time scale τ on the channel dimensions. For instance, in a viscoelastic Kelvin-Voight material driven to contract by a constant applied stress, $\tau = \eta$/E depends solely on the viscosity η and the Young's modulus E and is independent of the size of the channel[73]. In contrast, in a poroelastic material driven by a constant stress, $\tau \propto W_0^2$[74], where W_0 is the width of the channel. Thus, studying how τ varies with channel width provides a means to test

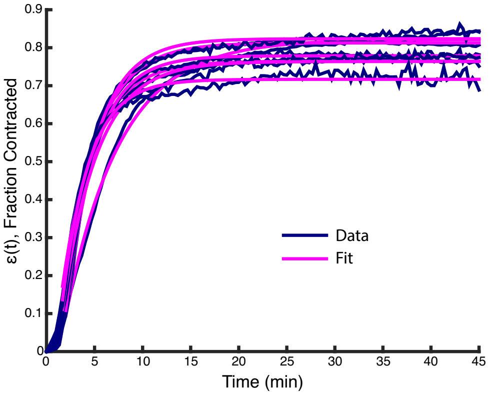

Figure 2.3: Plots of ϵ(t) from data in Fig 2.1 F (Blue lines) along with fits from Eqn. 2.2 (Pink lines).

the validity of these models.

We fabricated microfluidic channels of varying width, $W_0 = 1.4$mm, 0.9mm, 0.44mm, and 0.16 mm, all with height $H_0 = 125\ \mu$M, loaded the channels with extracts supplemented with 2.5 μM Taxol, and imaged the networks at low magnification (Fig 2.4 A). Results for each channel width were averaged together to produce master curves of the width, W(t) (Fig 2.4 B), and fraction contracted, ϵ(t) (Fig 2.4 C), of the networks in each channel. Visual inspection of the fraction contracted curves, ϵ(t), reveals that networks in smaller channels contract faster, but all reach a similar final fraction contracted (Fig 2.4 C). To quantify these trends, we fit the ϵ(t) curves using Eqn. 2.2 and extracted the characteristic time to contract, τ , and the final fraction contracted, ϵ_∞, for each channel width. We find that the dependence of τ on channel width is inconsistent with the time of contraction resulting from either viscoelastic or poroelastic timescales, which would predict constant and quadratic scalings respectively (Fig 2.4 D). We next explored the influence of channel height H_0 ($H_0 = 75$, 125, 150μM, all with width $W_0 = 1.4$ mm) and found that τ does not significantly

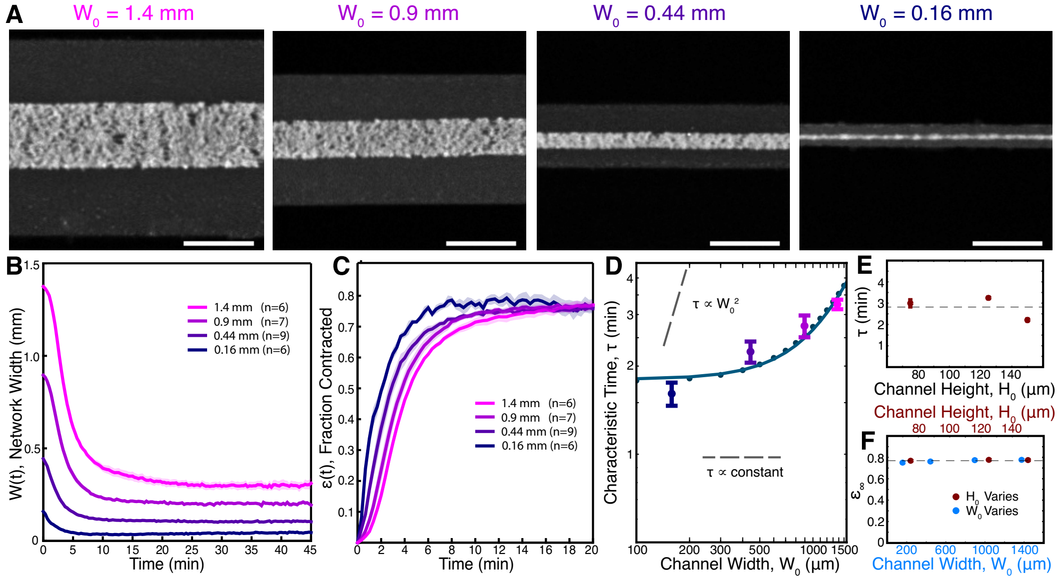

Figure 2.4: Contraction dynamics in channels of different width provide a means to test potential contraction mechanisms. (A) Microtubules form contractile networks in channels with various widths (Scale bar, 500 μm, t=10 minutes) (B) Width of the networks as a function of time in channels with various widths. (C) Fraction contracted as a function of time, ϵ(t), calculated from the data in B. The networks all contract to a similar final fraction, while the timescale of contraction differs. (D) The scaling of the characteristic time, τ, with channel width does not vary as W_0^2, as would result for a poroelastic timescale, and is not a constant, independent of width, as would result from a viscoelastic time scale. The scaling is well described by an active fluid model (green line analytic scaling, fit to Eqn. 2.6; green dots numerical solution). (E) The characteristic time, τ, is found to be independent of channel height. The dashed line is the mean value of τ. (F) ϵ_∞ is constant for all channel widths and heights, indicating that the network contracts to a constant final density. The dashed line is the mean value of ϵ_∞. All panels display mean ± s.e.m.

vary in these channels (Fig 2.4 E).

In all cases the networks contracted to a similar final fraction, ϵ_∞, of ≈ 0.77, irrespective of channel geometry (Fig 2.4 F). Since the Taxol concentration was held constant, all experiments started with the same initial density of microtubules, regardless of the dimensions of the channel. Thus, all networks contracted to the same final density. By using fluorescence intensity as a proxy for tubulin concentration (Materials and Methods), we estimate the final concentration of tubulin in the network to be $\rho_0 \approx 30\mu$M. Remarkably, this is comparable to the concentration of microtubules in reconstituted meiotic spindles in *Xenopus* extracts[75], which is $\approx 60\mu$M. As neither the simple viscoelastic nor poroelastic models are consistent with these results, we sought to construct an alternative model of the contraction process. Since Taxol stabilizes microtubules in these experiments, the density of microtubules ρ is conserved throughout the contraction process, implying

$$\partial_t \rho = -\vec{\nabla} \cdot (\rho \vec{v}), \tag{2.3}$$

where $\vec{v}$ is the local velocity of the microtubule network. The velocity $\vec{v}$ is set by force balance. If the relevant timescales are long enough that the microtubule network can be considered to be purely viscous, and if the network's motion results in drag, then the equation for force balance is

$$\eta \nabla^2 \vec{v} - \gamma \vec{v} = \vec{\nabla} \cdot \sigma, \tag{2.4}$$

where η and γ are the viscosity and drag coefficients, respectively, and σ is an active stress caused by motor proteins which drive the contraction of the microtubule network. The observation that the timescale of contraction, τ, is independent of chan-

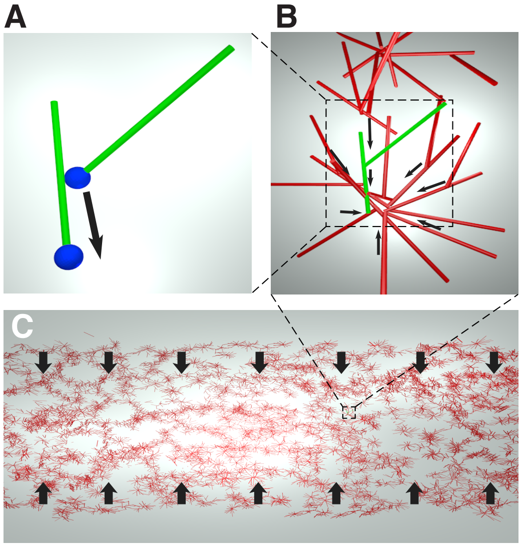

Figure 2.5: Cartoon of the microscopic model underlying the active fluid theory of network contractions by minus end clustering. (A) Microtubule sliding by dynein drives microtubule minus ends together. (B) Minus end clustering leads to the formation of aster-like structures. Due to steric interactions between microtubules, there is an upper limit to the local microtubule density. (C) The microtubule network is composed of interacting asters. Motor activity driving aster cores together leads to bulk contraction of the network.

nel height (Fig 2.4 E) shows that the drag does not significantly vary with channel height, and thus could arise from weak interactions between the microtubule network and the device wall.

We obtain an expression for the active stress, σ, by considering the microscopic behaviors of microtubules and motor proteins. As the contracting networks consist of microtubule asters (Fig 2.1 D, E), and microtubule asters in meiotic extracts are thought to assemble by the dynein-induced clustering of microtubule minus ends[29], we hypothesize that the contraction process is also driven by dynein pulling microtubule minus ends towards each other (Fig 2.5 A).

In an orientationally disordered suspension of microtubules, we expect dynein mediated collection of microtubule minus ends to drive a contractile stress which is proportional to the number of motor molecules m and the local density of microtubules ρ, (see Appendix B).

As only a finite number of microtubules can fit near the core of an aster, steric collisions will counteract the contractile stress at high densities (Fig 2.5 B).

Since most motion in the suspension is motor driven, thermal collisions can be ignored, and the extensile stress driven by steric interactions will be be proportional to the number motor molecules m and quadratic in the local density of microtubules ρ, (see Appendix B).

Taken together, these two effects lead to the active stress

$$\sigma = s\rho(\rho - \rho_0)\mathbb{I}, \tag{2.5}$$

where s is the strength of the active stress, ρ_0 is the final density at which the effects of dynein mediated clustering and steric repulsion between microtubules balance and $\mathbb{I}$ is a unit tensor (see Appendix B).

Importantly, since the contractile and extensile parts of the active stress both depend linearly on the number of motor molecules, the prefered density ρ_0 that the suspension will reach after contraction depends only on the interaction geometry between microtubules and motors and not on the actual number of active motors. Only the strength s of the active stress will be affected if the number of active motors could be changed.

Taken together, Eqns. (2.3, 2.4, 2.5) constitutes an active fluid theory of microtubule network contraction by minus end clustering. We note that this theory could be reformulated, essentially without change, as the clustering of aster cores, again driven by dynein mediated clustering of minus-ends. Isotropy of interactions remains a fundamental assumption.

We first investigated if this active fluid theory can explain the dependence of the timescale of contraction on sample geometry. An analysis of the equations of motion, Eqns. (2.3, 2.4, 2.5), near equilibrium predicts that the timescale of contractions obeys

$$\tau(W_0) = \alpha \frac{\eta}{s\rho_0^2} + \beta \frac{\gamma}{s\rho_0^2} W_0^2, \tag{2.6}$$

where $\alpha = 2.2 \pm 0.05$ and $\beta = 0.085 \pm 0.006$ are dimensionless constants, which we determined numerically (see Appendix B). This predicted scaling is both consistent with the experimental data and simulations of the full theory (Fig 2.4 D). Fitting the scaling relationship to the data allows combinations of the parameters to be determined, giving $\eta/(s\rho_0^2) = 0.82 \pm 0.20$ min and $\gamma/(s\rho_0^2) = 1.0\ \times 10^{-5} \pm 0.7 \times 10^{-5}$ min/(μm^2) (mean ± standard error). Combining this measurement with an estimate for the network viscosity taken from measurements in spindles of $\eta \approx 2 \times 10^{-2} Pa \cdot s$[76], we can estimate the dynein generated active stress to be $s\rho_0^2 \approx 4Pa$ which is consistant with having ≈ 0.4 dynein per microtubule minus end each exerting an average force of 1 pN[77].

To further explore the validity of the active fluid theory of contraction by microtubule minus end clustering, we explored other testable predictions of the theory. This theory predicts that: (i) the preferred density of the network ρ_0 is constant and does not depend on the initial conditions. This is consistent with the constant ϵ_∞ measured experimentally (Fig 2.4 B); (ii) since contractions are driven by stress gradients (Eqn 2.4) and stress depends on microtubule density (Eqn 2.5) the density discontinuity at the edge of the network should produce large stress gradients, leading

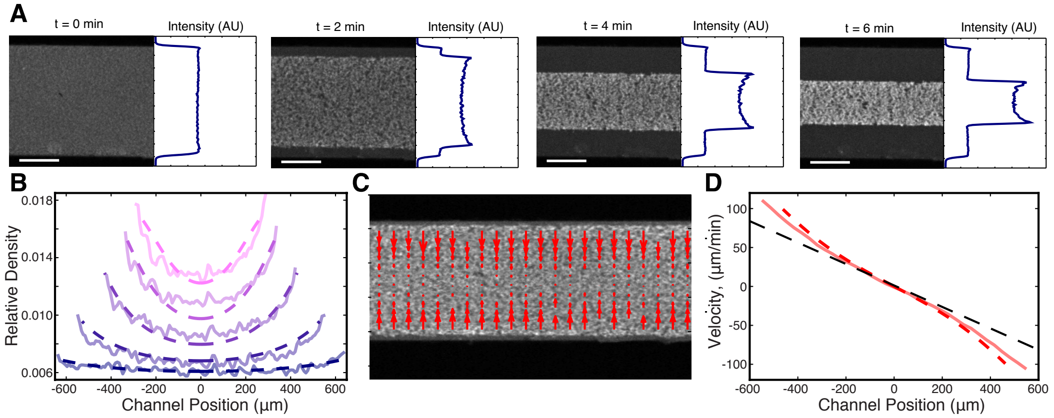

Figure 2.6: Microtubule density increases at the network's edges during contraction. (A) Time series of contraction showing intensity averaged along the length of the channel. The average intensity peaks at the network's edges due to increased local microtubule density. (Scale bars, 500 μm) (B) Comparison of measured density profiles (solid lines) with density profiles from simulation (dashed lines). Data are plotted at 1 minute intervals starting at t = 40 sec. (C) Representative frame from PIV showing the network's local velocity component along the network's width. (D) Comparison between measured (solid red line) and simulated (dashed red line) velocity along the width of the channel at t = 80 sec. The measured and simulated velocities increase superlinearly with distance from the center of the network, as can be seen by comparison to a linear velocity profile (dashed black line).

to an inhomogeneous density profile in the network during contraction; (iii) the magnitude of the active stress, s, is proportional to the number of active motors, but the final density of the network, ρ_0, is independent of the number of molecular motors (see Appendix B). Thus, reducing the numbers of motors should lead to slower contractions, but still yield the same final density.

We first examined prediction (ii), that the stress discontinuity at the edge of the network should lead to a material buildup in the film. To test this, we averaged the fluorescence intensity along the length of the channel (see Appendix C) and found that the microtubule density does indeed increase at the network's edge during contraction (Fig 2.6 A). We next explored if the inhomogeneous density profile could be quantitatively explained by our active fluid theory. We numerically solved Eqns 2.3,

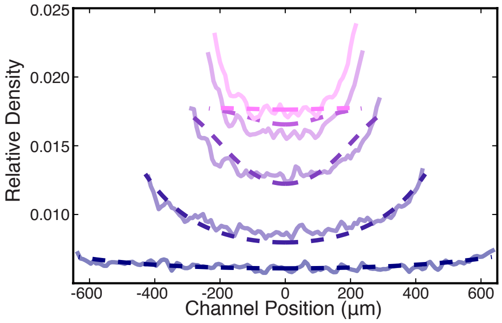

Figure 2.7: Comparison between measured (solid lines) and simulated (dashed lines) density profiles. Data are plotted at 2 minute intervals starting at t = 40 sec. (Pink lines).

2.4, and 2.5, and used least squares fitting to determine the simulation parameters which most closely matched the experimentally measured profiles (Fig 5B), yielding $\eta/(s\rho_0^2) = 0.82\pm0.03$ min, $\gamma/(s\rho_0^2) = 6.1\pm0.1\times10^{-6}$ $\text{min}/(\mu m^2)$, and $\rho_{initial}/\rho_0 = 0.32 \pm 0.01$ (mean ± s.e.m., n=4 experiments). Within error, these values are the same as those determined from the dependence of the timescale of contraction on channel width (Fig 2.4 D). The simulated profiles closely match the experimental ones for most of the contraction (Fig 2.6 B), but at late times the simulated inhomogeneities dissipate in contrast to the experiments (Figure 2.7). This might be caused by a long-term aging of the network that is not incorporated into our simple model. To confirm that the density buildup was due to an increased velocity near the network's edge, we measured the velocity throughout the network using Particle Image Velocimetry (PIV, see Materials and Methods) (Fig 2.6 C) and found that the velocities increase superlinearly with distance from the network's center, as predicted (Fig 2.6 D).

Finally, we sought to determine the molecular basis of the contraction process, and check prediction (iii), that the number of motors driving the contraction affects the rate of contraction, but not the final density the network contracts to. Aster assem-

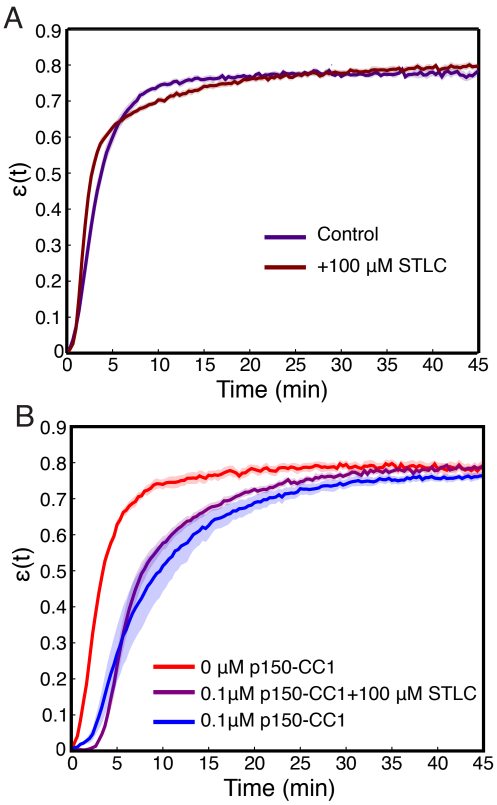

Figure 2.8: Inhibition of Kinesin-5 has little effect on the contraction process. (A) Comparison of $\epsilon(t)$ curves for samples where Kinesin-5 was inhibited using STLC and control where no STLC was added. (B) Simultaneous inhibition of dynein with p150-CC1 and Kinesin-5 with STLC does not rescue the effects of dynein inhibition alone. All panels display mean ± s.e.m.

bly is dynein-dependent in *Xenopus* egg extracts[29,71], and dynein[2] and Kinesin-5[3] are two of the most dominant motors in spindle assembly in this system. We inhibited these motors to test their involvement in the contraction process. Extracts supplemented with STLC for Kinesin-5 inhibition or p150-CC1 for dynein inhibition were loaded into channels with a width, W_0, of 0.9 mm and imaged at low magnification. Inhibiting Kinesin-5 had little effect on the contraction process (Figure 2.8). In contrast, inhibiting dynein caused a dose-dependent slowdown of the contraction (Fig 2.9 A). In spindle assembly, inhibiting Kinesin-5 suppresses the morphological changes caused by dynein inhibition[4]. We therefore tested how simultaneously inhibiting both motors influences the contraction process, but found that the effects of dynein inhibition were not rescued by the simultaneous inhibition of Kinesin-5 (Figure 2.8), suggesting that in this context, Kinesin-5 is not generating a counteracting extensile stress. This further suggests the possibility that in the spindle, the role of Kinesin-5 may be in orienting, polarity sorting, and sliding microtubules as opposed to active stress generation. Curves of ϵ(t) were fit using Eqn. 2.2 to extract the final fraction contracted, ϵ_∞, and the characteristic time of contraction, τ. By varying the concentration of p150-CC1, the characteristic time, τ, could be tuned over a wide range from $\approx$ 3 minutes to $\approx$ 75 minutes (Fig 2.9 B). Fitting a sigmoid function to the τ vs. p150-CC1 concentration curve yields an EC50 value of 0.22 $\pm$ .02 μM (mean $\pm$ standard error), similar to the value of $\approx$ 0.3 μM reported for the effect of p150-CC1 on spindle length in *Xenopus* extracts[6], which is consistent with active stress generated by dynein being required for pole focusing. Despite this large change in the contraction timescale, we found no apparent differences in ϵ_∞ (Fig 2.9 C). Thus, the microtubule networks contract to approximately the same final density irrespective of the concentration of p150-CC1. The observation that inhibiting dynein affects the

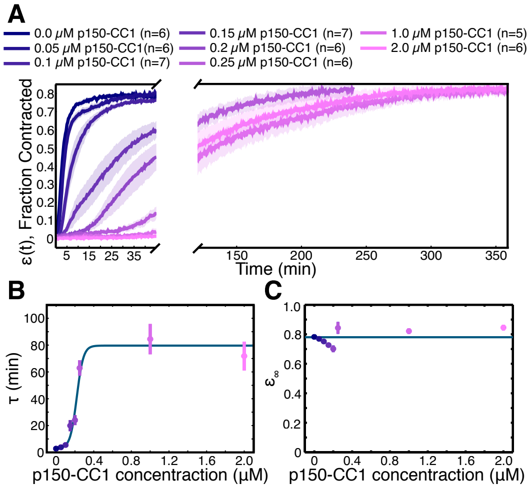

Figure 2.9: Network contraction is a dynein-dependent process. (A) Fraction contracted as a function of time, ϵ(t), when dynein is inhibited using p150-CC1. (B) The characteristic time of contraction, τ, increases with increasing p150-CC1 concentration. Solid green line indicates fit of sigmoid function. (C) ϵ_∞ has no apparent variation with p150-CC1 concentration. Solid green line indicates the mean value of ϵ_∞. All panels display mean ± s.e.m.

timescale of contraction but not the final density to which the network contracts is consistent with the predictions of our model. We note that even at the highest p150-CC1 concentrations used, the network still undergoes a bulk contraction. This could possibly be due to incomplete inhibition of dynein by p150-CC1, or by another motor protein present in the extract that also contributes to the contraction process. As the characteristic time, $\tau \propto \frac{1}{s}$, by comparing the characteristic times in the uninhibited and 2 μM p150-CC1 cases, we can estimate that the strength of the active stress, s, in the 2 μM p150-CC1 condition is only $\approx 4\%$ of the strength of the active stress in the uninhibited case, arguing that even if another motor is involved in the contraction, dynein contributes $\approx 96\%$ of the active stress.

2.3 Discussion

Here we have shown that networks of stabilized microtubules in *Xenopus* egg extracts undergo a bulk contraction. By systematically varying the width of the microfluidic channel in which the network forms, we demonstrated that the timescale of contraction is not a poroelastic or viscoelastic timescale. A simple active fluid model of network contraction by dynein-driven clustering of microtubule minus ends correctly predicts the dependence of the contraction timescale on channel width, the nonuniform density profile in the network during contraction, and that inhibiting dynein affects the timescale of contraction but not the final density that the network contracts to. Parameters of this model can be measured by the scaling of the contraction timescale with channel width and by a detailed analysis of the inhomogeneities in the network that develop during contraction. Both methods give similar values.

Our results demonstrate that the behaviors of a complex biological system can be quantitatively described by a simple active matter continuum theory. These active matter theories aim to describe the behavior of cytoskeletal systems at large length-scales and long timescales by effectively averaging all of the molecular complexity into a small set of coarse-grained parameters. Previously, these theories have been predominately applied to describe biological systems near non-equilibrium steady states[56,60]. In the present work, we augment previous theories with a nonlinear active stress term derived from microscopic considerations to capture the far from steady state dynamics of the contraction process. This approach allows us to quantitatively explain our experimental results using a theory with only 4 parameters, while a complete microscopic model would require understanding the behavior of the thousands of different proteins present in *Xenopus* egg extracts. Furthermore, the considerations of the model are general, and it will be interesting to consider whether the end clustering mechanism proposed here could contribute to contraction in actin networks as well.

In our model, the active stress which drives network contraction results from the motor-induced clustering of microtubule minus ends, the same process thought to be responsible for aster formation and spindle pole focusing[29,71,2,78,32,10,31,79]. Our results, and previous data[29,2,10], are consistent with minus end clustering in *Xenopus* egg extracts primarily arising from the activity of dynein. The ability of dynein to cluster microtubule minus ends could result from dynein being able to accumulate on the minus end of one microtubule, while simultaneously walking towards the minus end of another[11,23]. There is indication that such behaviors may indeed occur in spindles[32], and pursuing a better understanding of those processes is an exciting future direction that will help to clarify the function of dynein in spindles.

The observation that microtubule networks contract in *Xenopus* egg extracts suggests that motor-induced stresses in spindles are net contractile and not extensile as previously assumed[60]. The contribution of dynein to spindle pole focusing may ultimately be due to these contractile stresses. The presence of contractile stresses from dynein might also explain both the observation that the fusion of spindles is dynein-dependent[1], and the apparently greater cohesion between microtubules at spindle poles, (where dynein is localized[80]). It is unclear what processes set the density of microtubules in the spindle, and the finding that the active stress generated from minus end clustering saturates at a preferred microtubule density could play an important role.

3

Connecting macroscopic dynamics with microscopic properties in active network contraction

3.1 Introduction

Active matter is a class of materials help out of equilibrium by the local conversion of energy into directional motion at the scale of the system's components[40]. These active matter systems frequently exhibit emergent, collective behaviors and pattern formation on length scales much larger than the size of the system's constituent components. Cytoskeletal networks, composed of polar polymeric filaments held out of equilibrium by forces produced by molecular motor proteins, are examples of living active matter[56]. Within cells, cytoskeletal networks are responsible for a number of cellular functions, including cell division and chromosome segregation. Networks of cytoskeletal active matter have been studied experimentally, both in purified systems[62,81] and in biological systems of cells and cell extracts[30,60,82,83]. Understanding how the dynamics and architecture of these networks emerges from the properties of the cytoskeletal filaments and motor proteins the networks are composed of is an open question not fully addressed for any cytoskeletal system.

In the previous chapter we showed that in meiotically-arrested *Xenopus* oocyte extracts, networks of stabilized microtubules undergo a spontaneous bulk contraction, driven by the clustering of microtubule minus ends by the motor protein dynein[30]. Experimental results were in quantitative agreement with an active fluid model, which makes several predictions, including that the networks will contract to a preferred final density regardless of sample geometry and motor concentration.

Here, we further test the model by measuring the effects of varying the initial microtubule density and the length distribution of the microtubules by varying the amount of taxol used to nucleate, polymerize, and stabilize the microtubules. Consistent with previous results, we find that when taxol concentration is increased, both the mass density and the number density of microtubules increase while the average length of the microtubules decreases. Consistent with predictions of our active fluid model, we find that the final density of these networks is approximately constant. Intriguingly, we also find that the characteristic timescale of the contraction process increases with increasing taxol concentration. This trend continues, even in the regime of high taxol concentration, where the initial density of polymerized microtubules is approximately constant, arguing that the increase in contraction timescale doesn't result from an increase in the initial network density. We further find that the average microtubule length decreases with increasing taxol concentration. Taken together, these results suggest that the contraction timescale may be influenced by the microtubule length distribution. Further work will be necessary to connect these macroscopic network dynamics with the microscopic properties of the network's constituent microtubules.

3.2 RESULTS

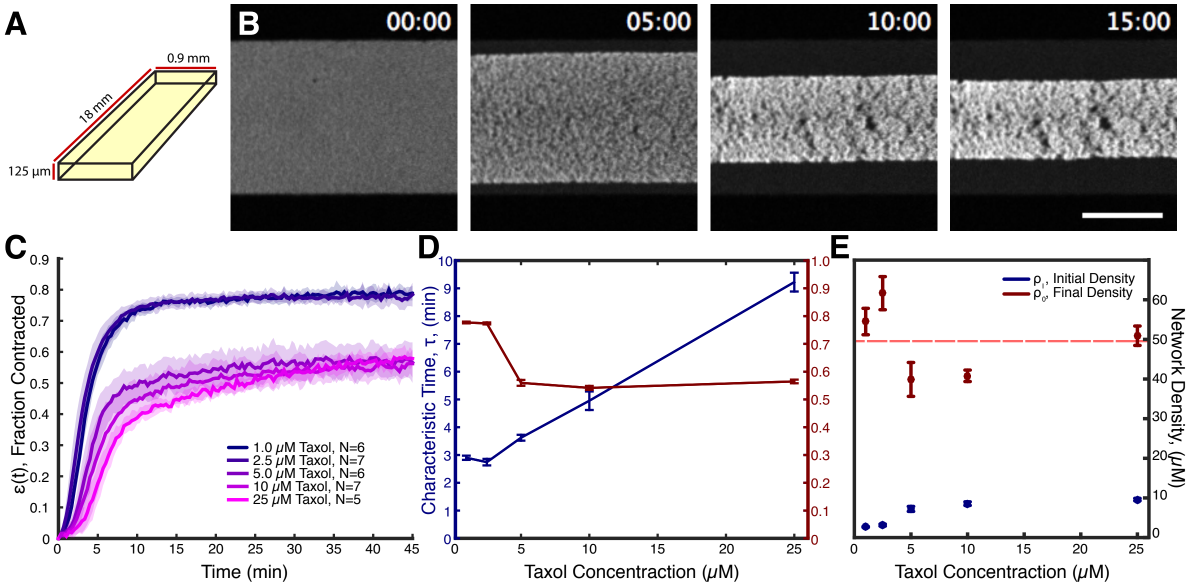

Figure 3.1: (A) Schematic showing characteristic dimensions of the microfluidic chamber. (B) Time course of microtubule network contraction when 10 μM taxol is added (Scale bar: 500 μm) (C) Curves showing the fraction contraction, ϵ(t) as a function of time for varying taxol concentration. Curves are mean ± s.e.m. (D) Characteristic time, τ, and final fraction contraction, ϵ_∞, as a function of taxol concentration. (E) Initial network density, ρ_I, (blue dots) and final network density, ρ_0, (red dots) as a function of taxol concentration. The red dashed line denotes the average value of the final network density, ρ_0=49.6 μM .

To further investigate the dynamics of contracting microtubule networks in *Xeno-*

pus oocyte extracts, we added taxol to the extracts in order to polymerize endogenous tubulin into stabilized microtubules, as previously described[30]. These extracts were loaded into rectangular microfluidic devices (Figure 3.1A), sealed at the inlet and outlet using vacuum grease to prevent evaporation, and imaged at low magnification (Materials and Methods). Within minutes, the microtubule networks were found to undergo a spontaneous bulk contraction (Figure 3.1B). To quantify the dynamics of the contraction process, the size of the network along the width of the channel, $W(t)$, was measured as a function of time, and converted to the fraction the network contracted, $\epsilon(t)$, using the relation,

$$\epsilon(t) = \frac{W_0 - W(t)}{W_0} \tag{3.1}$$

where W_0 is the width of the channel, typically 0.9 mm. This process was repeated for varying concentrations of added taxol. $\epsilon(t)$ curves for each taxol condition were found to be similar, and thus these curves were averaged together in order to produce master curves for each condition (Figure 3.1C). As in the previous chapter, $\epsilon(t)$ curves were found to be well fit by a saturating exponential function,

$$\epsilon(t) = \epsilon_\infty[1 - e^{-(\frac{t-T_c}{\tau})}] \tag{3.2}$$

where ϵ_∞ is the final fraction contracted, τ is the characteristic contraction time, and T_c is a lag time between the beginning of imaging and the beginning of the the contraction process. Eqn. 3.2 was fit to the measured $\epsilon(t)$ curves for each experiment, and these fits were used to extract values for the characteristic time, τ, and the final fraction contracted, ϵ_∞, which were then averaged for each taxol condition (Figure 3.1D). The characteristic timescale, τ, was found to increase approximately linearly for taxol concentrations >2.5 μM, while the final fraction contracted, ϵ_∞, decreases with increasing taxol concentration (Figure 3.1D).

In systems of purified tubulin, the concentration of tubulin polymerized into microtubules has been shown to increase with increasing taxol concentration[84]. We next investigated how changing taxol concentration influences both the initial density of the microtubule network, ρ_I, and the final density of the microtubule network, ρ_0. Fluorescence intensity was used as a proxy for tubulin concentration, and was calibrated using previously measured values for the total tubulin concentration in *Xenopus* extracts (Materials and Methods). While the initial density of the microtubule network, ρ_I, monotonically increased with increasing taxol concentration, the final density of the microtubule network displayed no obvious trend (Figure 3.1E), and values of the final network density vary from the mean final density of ρ_0= 49.6 μM by less than 25%. This is consistent with the results presented in the previous chapter arguing that contracting microtubule networks in *Xenopus* extracts contract until they reach a preferred final density[30]. While the initial microtubule density, ρ_I, increases with increasing taxol concentration, this increase appears to saturate for large taxol concentrations. Considering the three largest taxol concentrations investigated here (5 μM, 10 μM, and 25 μM), the initial microtubule densities was found to vary to vary from the mean value by only 14% (std/mean), far less than the $\approx 2.5\times$ increase seen in the contraction timescale, τ, over this same range. Thus, the characteristic contraction timescale, τ, does not scale proportionally to the initial density of microtubules, ρ_I, and the change in contraction timescale must come from some other effect of changing taxol concentration.

Previously, it has been shown that the size of motor-organized taxol-stabilized microtubule assemblies termed ”pineapples” in clarified *Xenopus* extracts decreases with

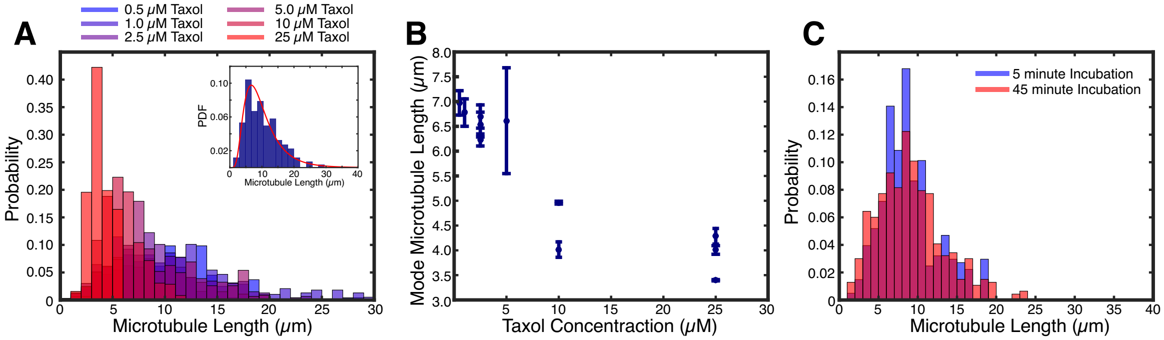

Figure 3.2: (A) Histograms of microtubule lengths measured for differing taxol concentrations. Inset: Example distrubution for 2.5 μM taxol with log-normal fit (red line). (B) The mode microtubule length decreases with increasing taxol concentration. (C) Example histograms for 2.5 μM taxol, where microtubule networks were dissociated and fixed at either 5 minutes or 45 minutes after taxol addition.

increasing taxol concentration, presumably due to a decrease in the average lengths of microtubules[70]. Thus, we next sought to measure the length distribution of microtubules in our system for varying taxol concentration. We used a previously described method to dissociate and fix microtubules[70] (Materials and Methods). Briefly, microtubules were allowed to assemble for 5 minutes after taxol addition before being diluted into a dissociation buffer containing 250 mM NaCl, which dissociates motor proteins and other MAPs from the microtubules. After a 2 minute incubation, this mix was diluted again into a fixation buffer containing glutaraldehyde. Microtubules were fixed for 5 minutes, further diluted, and thinly spread between a slide and a 22 mm^2 coverslip. Microtubules were allowed to adhere for 30 minutes before imaging. An active contour was fit to microtubules in the images[85], and the length of the active contour was used as a measure for the microtubule length. This process was repeated for each taxol concentration.

Example histograms of microtubules lengths for each taxol concentration are shown in Figure 3.2A. Visually, the peak of the distribution shifts towards smaller values of microtubule length for increasing taxol concentration. Empirically, we find that the distributions of microtubule lengths are well fit by a log-normal distribution (Figure 3.2A, Inset). As fitting log-normal distributions to the measured histograms allows a more robust estimate of the mode microtubule length than using a purely empirical estimate, we fit the microtubule length distributions for each taxol concentration in order to find μ and σ, the two parameters of the log-normal distribution, and used these parameters to estimate the mode microtubule length for each condition. The mode microtubule length was found to decrease with increasing taxol concentration, varying by a factor of ≈ 1.7 across the taxol conditions measured (Figure 3.2B).

One potential concern is that the microtubule length distribution may vary over the 45 minute timescale of the contraction experiments. Potentially, this could be due to a number of factors, including microtubule depolymerization, severing of microtubules, or other causes. To address this issue, we repeated our length distribution measurement where microtubule dissociation and fixation began 45 minutes after taxol addition. We find close agreement between the microtubule length distributions measured either 5 minutes or 45 minutes after taxol is added, indicating that the length distribution is approximately constant over the timescale of the contraction experiments (Figure 3.2C).

3.3 DISCUSSION

Here, we examined how the dynamics of bulk microtubule network contraction in *Xenopus* extracts vary with taxol concentration. We find that using different taxol concentrations, the networks contract to approximately the same final density, even though the initial density of the networks varies by a factor of ≈ 3.6. While the final density of these networks is constant, we find that the timescale of the contraction process increases with increasing taxol concentration. In the high taxol regime, where the initial network density varies by only ≈ 14%, we find that the timescale increases by a factor of ≈ 2.5, arguing that the timescale is not simply varying proportionally to the initial network density. The length distributions of the microtubules were measured for each taxol condition, and it was found that the average microtubule length decreases with increasing taxol concentration by a factor of ≈ 1.7 across the tested conditions.

The results presented here suggest that the timescale of the contraction process could be set, at least in part, by the length distribution of the microtubules that make up the network. Different ideas could potentially explain this phenomenom. From a macroscopic perspective, mechanical properties of crosslinked polymer[86] and cytoskeletal[87] networks have been shown to be strongly influenced by the length of the network's filaments. This could be due, in part, to longer microtubules having more available sites to crosslink with other microtubules, and hence longer microtubules being connected to more additional microtubules on average than shorter ones. In the previous chapter, we showed that the timescale of the contraction process contains a term proportional to the internal viscosity of the network, which could potentially change with microtubule length through this mechanism. It remains unclear whether or not the change in timescale can be fully explained by changes in the microtubule length distribution, and if so how these changes in the length distribution influence the bulk mechanical properties of the networks. Testing these ideas will be the grounds for future work.

4

In vitro microtubule network contraction by purified dynein complexes

4.1 Introduction

In the previous chapters we have shown that networks of stabilized microtubules in *Xenopus* oocyte extracts undergo a spontaneous bulk contraction on the millimeter length scale. We propose that the contraction process is fundamentally driven by the clustering of microtubule minus ends by the motor protein dynein. However, *Xenopus* extract is a biochemically complex environment, containing other microtubule motor proteins and crosslinkers in addition to dynein. Here, we test whether or not the dynein complex alone is truly sufficient to induce bulk contractions in networks of stabilized microtubules. In this chapter, we address this question using a system of stabilized microtubules and a purified, active form of the dynein complex.

In vivo, dynein's activity is regulated in part by accessory proteins, such as Lis1[25] and dynactin[88], that bind to the complex and modulate its properties. Here, we utilize a recently described active form of the dynein complex containing both dynactin and BicD2. Unlike purified mammalian dynein alone, complexes of dynein, dynactin, and BicD2, hereafter referred to as DDB, are processive *in vitro*, with an average run length > 8 μm[23]. *In vitro*, DDB has been shown to accumulate on microtubule minus ends[23], qualitatively recapitulating the accumulation of dynein on microtubule minus ends thought to occur in *Xenopus* extracts[29,30]. For these reasons, and as the proposed mechanism for microtubule network contraction is thought to fundamentally result from the accumulation of dynein at microtubule minus ends[30], we use this active form of DDB here. We show that DDB is sufficient to induce bulk network contraction in a system of purified microtubules. We further show that, as in extract, these contracting networks consist of networks of interacting asters. Finally, we test the effects of DDB concentration on both the timescale of the contraction process as well as the final fraction the network contracts.

4.2 RESULTS

Rectangular microfluidic devices of height 125 μm, width 0.9 mm, and length 18 mm were prepared and passivated as previously described[30]. Taxol stabilized microtubules containing either Alexa-647 or Atto-647 labeled tubulin were prepared fresh daily as previously described[89] at a final tubulin concentration of 18.9 μM. Purified mammalian DDB complex was a generous gift from Ruensern Tan and Richard McKenney

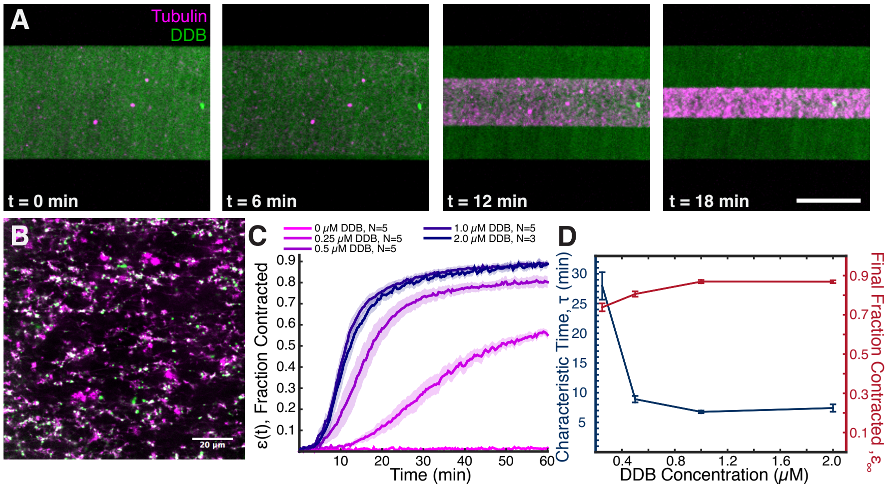

Figure 4.1: (A) Networks of stabilized microtubules and DDB undergo spontaneous bulk contraction. (Scale bar 500 μm) (B) High-mag imaging of the contracting networks, showing aster-like structures, with dynein localizing towards the interior. (Magenta: Tubulin ; Green DDB)(C) Average fractional network contraction as a function of time for varying DDB concentration. (D) Characteristic time, τ, and final fraction contracted, ϵ_{∞}, from fits to ϵ(t) curves as a function of DDB concentration.

and was purified as previously described[23] with a fluorescent TMR label attached to BicD2. This allowed DDB to be imaged in addition to the microtubules. Unless otherwise noted, the reaction buffer consisted of 1 μM DDB, taxol stabilized microtubules at a final tubulin concentration of 0.95 μM, 2.5 mM ATP, 20 % DMSO, and 20 μM taxol in Buffer A[23]. This mix was loaded into the microfluidic device which was then sealed with vacuum grease before imaging. When imaged at low magnification, we find that the microtubules undergo a spontaneous bulk contraction on the millimeter length scale that is strongly reminicent of the bulk contractions seen in *Xenopus* extracts (Figure 4.1A). Imaging of the contracting networks at high magnification showed that the microtubules in the network are organized into aster-like structures, with dynein localized in foci towards the interior of the aster-like structures, once again consistent with the fine structure of the contracting networks previously seen in *Xenopus* extracts (Figure 4.1B). In order to quantitatively extract parameters of the contraction dynamics, the width of the network as a function of time, $W(t)$, was measured for each experiment. As was done in previous chapters, these $W(t)$ measurements were converted to the fraction the network has contracted as a function of time, $\epsilon(t)$ using,

$$\epsilon(t) = \frac{W_0 - W(t)}{W_0} \tag{4.1}$$

where W_0 is the initial width of the network. These $\epsilon(t)$ curves were found to vary little for each condition, so $\epsilon(t)$ curves for individual experiments were averaged together to produce master curves for each condition (Figure 4.1C).

As in the network contractions in *Xenopus* extract, these $\epsilon(t)$ curves were well fit by a saturating exponential function,

$$\epsilon(t) \simeq \epsilon_\infty[1 - e^{\frac{-(t-T_c)}{\tau}}] \tag{4.2}$$

allowing τ, the characteristic contraction timescale, and ϵ_∞, the final fraction contracted to be measured for each experiment (Figure 4.1D).

Our active fluid model makes predictions about the effects of motor concentration on the dynamics of the contraction process. Namely, the model predicts that as motor concentration is reduced, the strength of the active stress is reduced and thus the characteristic contraction timescale, τ, increases. Meanwhile, the final density of the microtubule network, ρ_0, should remain unchanged with changing motor concentration. In the extract system, dynein was inhibited using p150-CC1, which inactivates dynein by competing with dynactin for binding sites. While the total amount of inhibitor could be titrated in the extracts and thus the amount of active dynein reduced

(Figure 2.9), the total amount of active dynein could not be quantitatively changed directly.

Here, using a system of purified microtubules and DDB, the total amount of DDB can be controlled. We thus repeated the experiments and analysis using DDB concentrations ranging from 0 μM to 2 μM, with all other parameters held fixed (Figure 4.1C, D). We find that for motor concentrations < 2 μM, the characteristic timescale of contraction, τ, increases with decreasing DDB concentration. Interestingly, for the 1 μM and 2 μM conditions, we find that both the characteristic timescale, τ, and the final fraction contracted, ϵ_{∞}, are indistinguishable between conditions (Figure 4.1D). We hypothesize that this is due to a motor saturation effect, as in both of these conditions the total concentration of DDB is greater than the total amount of tubulin dimers. Additionally, we also find that the final fraction contracted, ϵ_{∞}, slightly decreases with decreasing DDB concentration (Figure 4.1D). Since the initial density of microtubules is the same for all conditions, and the networks contract different fractions for varying DDB concentration, this argues that the final density of the network varies with DDB concentration. One possible explanation for this is that in this purified system, the final network density is influenced in part by a competition between active stresses generated by DDB and elasticity in the network. More work is necessary to follow up on this point.

4.3 Discussion

In summary, we have shown that the spontaneous bulk contraction of microtubule networks seen in *Xenopus* extracts can be recapitulated using a system of stabilized microtubules and a complex of dynein, dynactin, and BicD2. As was the case in *Xenopus* extracts, these DDB networks are composed of aster-like microtubule structures that are partially polarity sorted. These DDB network contractions have a single characteristic timescale, which was found to decrease with increasing DDB concentration. Intriguingly, we find that this decrease in timescale with increasing DDB concentration saturates when the DDB concentration is greater than the tubulin concentration. This argues that, at least for a given initial microtubule mass and length distribution, there exists a lower bound on the contraction timescale that can be achieved by varying the motor concentration. Whether this effect is due to a saturation of motor protein binding sites on the microtubules or due to some other effect remains unclear and would be an interesting area for future work.

The results presented here show that an active form of dynein alone is sufficient to drive bulk contraction of microtubule networks. These bulk contractions are seen using a motor protein complex that builds up on microtubule minus ends *in vitro*[23], and the fine structure of the contracting network was found to be a network of partially polarity sorted aster-like structures. These results are consistent with the generic ideas of our previously proposed model: that the bulk contraction of microtubule networks is driven by the motor-induced clustering of filament ends[30]. Additionally, recent results using the motor protein Eg5 and stabilized microtubules in a purified system have shown that in some conditions Eg5 can also cause both aster formation and bulk contraction of microtubule networks[90], though Eg5 was found to not contributed to network contraction dynamics in *Xenopus* extract (Figure 2.8). While the results our model are general, and multiple *in vitro* implementations of bulk network contraction have been seen, whether or not additional motor proteins can also cause bulk contraction of microtubule networks remains to be tested. Studying the similarities and differences between the contraction dynamics of networks composed of different motor proteins could potentially be a way to gain further insight into both the molecular-scale functions and the collective behaviors stemming from the activities of the motors.

5

A transition from contraction to extension in networks of microtubules and XCTK2

5.1 Introduction

In the previous chapters we have shown that networks of stabilized microtubules in *Xenopus* extracts undergo a spontaneous bulk contraction driven by the clustering of microtubule minus ends by dynein and that in a purified system, an active form of the dynein complex is sufficient to drive bulk contraction of networks of stabilized microtubules. Recent results have shown that in a different purified system, the motor protein Kinesin-5 is also capable of inducing bulk contraction of microtubule networks[90]. The presented active fluid model is generic, and predicts that any protein that clusters filament ends will lead to bulk network contraction. Here, we further test this idea using the motor protein XCTK2.

XCTK2 is a homologue of Kinesin-14 found in *Xenopus laevis*[91]. Kinesin-14 proteins are minus-end directed motor proteins capable of crosslinking and sliding microtubules *in vitro*[33,54,92]. In some systems, such as *Drosophila* female meiotic spindles, Kinesin-14 has been proposed to play an important role in focusing spindle poles, a functionally similar role to the role dynein plays in other organisms[54,93]. *In vitro*, Ncd, the *Drosophila* Kinesin-14 homologue, has been shown to accumulate on microtubule minus ends[33], and XCTK2 has been shown to be able to organize dynamic microtubules into asters[54]. For these reasons, we expect that XCTK2 could induce bulk contractions in networks of stabilized microtubules.

Here, we study the collective organization of networks composed of stabilized microtubules and XCTK2. We first confirm that XCTK2 can accumulate on microtubule minus ends and can organize microtubules into asters. We then show that networks of XCTK2 and microtubules undergo a spontaneous, uniform, bulk contraction. However, unlike the microtubule and motor protein networks previously considered, these networks transition to an extensile phase after the initial bulk contraction. We further show that during contraction, microtubules in the network align, building up nematic order. We then show that microtubules in the network undergo polarity sorting, and build up polar order. We hypothesis that this polarity sorting could give rise to the extensile phase, though further work will be necessary to quantitatively test

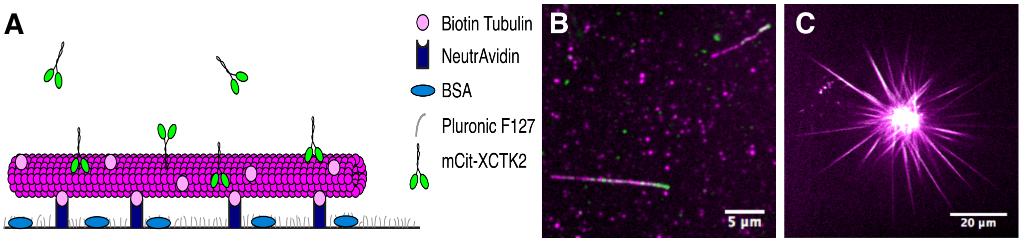

Figure 5.1: XCTK2 accumulates at microtubule minus ends and can form asters of stabilized microtubules. (A) Schematic of the experimental setup for end accumulation measurement. (B) XCTK2 builds up on the minus ends of stabilized microtubules Green: mCit-XCKT2 , Magenta: Tubulin (C) Example microtubule aster formed with XCTK2 at a final concentration of 500 μM. Green: mCit-XCKT2 , Magenta: Tubulin

this idea.

5.2 Results

We first investigated whether XCTK2 accumulates on the minus ends of stabilized microtubules. Taxol stabilized microtubules containing $\approx$ 8% biotin labeled tubulin and $\approx$ 8% Alexa-647 labeled tubulin were prepared as previously described[94]. Imaging chambers were made from slides and coverslips with NeutrAvidin attached to the surface and passivated with Pluronic-F127 and BSA[95] (Materials and Methods). The biotinylated microtubules were then added to the imaging chamber, where they strongly adhered to the NeutrAvidin on the surface (Figure 5.1A). Reaction mix composed of 1x Self-Organization Buffer, 20 μM taxol, and 100 nM mCit-XCTK2 (a generous gift of Stephanie Ems-McClung and Claire Walczak) was then added to the flow chambers. The chambers were then sealed with wax to prevent evaporation before imaging (Materials and Methods). Within minutes, XCTK2 was found to preferentially accumulate on one end of the microtubule, presumed to be the minus end as XCTK2 is a minus end directed motor protein (Figure 5.1B). Thus, like the

Drosophila homologue of Kinesin-14, Ncd[33], XCTK2 can accumulate on microtubule minus ends *in vitro*.

We next asked whether XCTK2 can organize stabilized microtubules into asters. A reaction mix consisting of 40 μM tubulin, 500 μM mCit-XCTK2, 20 μM taxol, Gloxy (to prevent photobleaching) 2 μM taxol, and PK-LDH and PEP (to regenerate ATP) in 1x Self-Organization Buffer was added to a 125 μm × 0.9mm × 18 mm passivated microfluidic chamber described in previous chapters (Materials and Methods) and imaged at high magnification. After $\approx$ 1 hour, microtubule asters were visible in some regions of the channel (Figure 5.1C). mCit-XCTK2 was found to accumulate towards the center of the asters, arguing that the asters are polarity sorted with their minus ends towards the core of the aster, conceptually similar to the dynein organized microtubule asters formed in *Xenopus* extract.

We next examined the large-length scale behavior of networks composed of stabilized microtubules and XCTK2. Sample chambers were designed with a 110 μm thick PDMS spacer bonded between a glass slide and coverslip (Materials and Methods). Unlike the previously used devices where the chamber was made of PDMS bonded to a coverslip, these new devices allow transmitted light to pass through, allowing diascopic imaging to be taken simultaneously. We take advantage of this by using a combination of epifluorescence imaging to measure tubulin fluorescence, which can be used as a proxy for tubulin density, and PolScope imaging, a form of quantitative polarized light microscopy that gives a measurement of the optical retardance[96]. Optical retardance provides a measure of birefringence in the sample, which can arise from the intrinsic birefringence of the microtubules and from form birefringence from the arrangement of microtubules in the network. Optical retardance scales proportionally to both the local density and the local alignment of filament arrays[97]. Thus, the

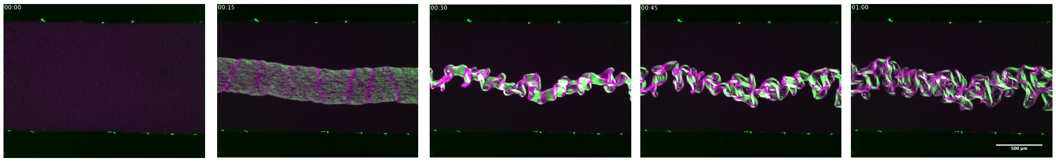

Figure 5.2: Networks containing 1 μM mCit-XCTK2 and taxol stabilized microtubules undergo a spontaneous bulk contraction followed by extension. Magenta: Tubulin Fluorescence ; Green: Optical Retardance. Time in hours:minutes.

PolScope measurements can be combined with the fluorescence measurements in order to provide a measure of the local alignment of microtubules in the networks.

At a mCit-XCTK2 concentration of 1 μM, microtubule networks undergo a spontaneous bulk contraction, (Figure 5.2). As the network contracts, the optical retardance signal increases, indicating that during network contraction, the microtubules are also aligning nematically. However, unlike any of the contractile networks described in previous chapters, the contracted state of the mCit-XCTK2 networks considered here appear to be unstable, and the networks begin to buckle and extend shortly after contraction (Figure 5.2).

We hypothesize that the initial contraction happens in a similar manner to the contractions seen previously: that XCTK2 accumulates and clusters microtubule minus ends into aster-like structures that fuse, causing bulk network contraction. Previous results have shown that when microtubules are aligned, XCTK2 accumulates in the overlap region[54], and that Kinesin-14 motors, including XCTK2, can slide antiparallel microtubules[33,54]. We hypothesize that during the contraction process, XCTK2 accumulates between aligned microtubules, crosslinking them together. This process leads to a global alignment of microtubules in the network. XCTK2 could then slide antiparallel microtubules relative to each other, which would polarity sort the microtubules in the network. This polarity sorting could give rise to the extensile active

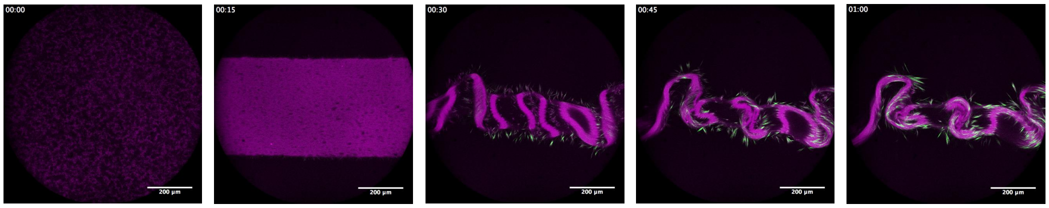

Figure 5.3: Networks containing 1 μM mCit-XCTK2 and taxol stabilized microtubules undergo a spontaneous bulk contraction followed by extension, and the network polarity increases during the extension phase. Magenta: Tubulin Fluorescence ; Green: SHG Signal. Time in hours:minutes.

stress which could cause the bulk extension in the network[41].

One prediction of this model is that the polarity of the network will increase with time as the network becomes more and more polarity sorted. To test this prediction, we next performed Second Harmonic Generation (SHG) measurements on networks containing 1 μM mCit-XCTK2. SHG is a nonlinear optical technique where the signal increases proportionally to both the local polarity of the microtubule network and to the square of the density of the network[98]. When combined with two-photon microscopy to provide a measure of microtubule density, SHG measurements provide a measure of the local polarity in the network as a function of space and time. Consistent with these ideas, we find that the SHG signal in the networks increases with time (Figure 5.3), arguing that the polar ordering of the network is increasing.

5.3 Discussion

Here, we've shown that, like Ncd[33], XCTK2 can accumulate on microtubule minus ends and that XCTK2 can organize taxol stabilized microtubules into asters. At a final XCTK2 concentration of 1 μM, networks of stabilized microtubules and XCTK2 undergo a bulk contraction followed by bulk extension. In these networks, the increase in network density happens concurrently with an increase in local alignment in the networks. Following the initial contraction, we find that microtubule polarity also increases in these networks. While the initial contraction of these networks can be understood in terms of the active fluid model based on the clustering of filament ends described in previous chapters, further work will be necessary to understand whether or not the network extension is driven by polarity sorting of microtubules by XCTK2.

6

Conclusions

Here, we've shown that networks of stabilized microtubules in *Xenopus* oocyte extracts undergo a spontaneous bulk contraction on the millimeter length scale. This contraction is fundamentally driven by the clustering of microtubule minus ends by dynein. An active fluid model of the contraction process was proposed that makes several predictions in quantitative agreement with experimental results, including the effects of sample geometry on contraction timescale, the shape of density inhomogeneities which develop during the contraction process, and the increase in contraction timescale when dynein is inhibited. The model also predicts that the networks contract to a constant final density independent of sample geometry, dynein concentration, or initial microtubule concentration which was again confirmed experimentally. We then showed that in a purified, *in vitro* system, an active form of the dynein complex containing dynein, dynactin, and BicD2 is sufficient to drive bulk contraction in networks of stabilized microtubules and that these contractions are qualitatively the same as the network contractions seen in *Xenopus* extracts. Finally, we showed that XCTK2, another minus end directed motor protein, can also cause bulk contractions of microtubule networks, which are followed by network extension.

Taken together, these results describe a generic mechanism that can lead to bulk network contractions: the clustering of filament ends. This mechanism allows for a connection between the bulk properties of the system and the microscope interactions between the system's components, and could potentially be a design principle for controlling the behavior of active systems. These results also suggest a tentative role for dynein in spindles: to generate contractile stresses. This mechanism could potentially explain, in part, what sets the density of microtubules within the spindle. Further work performed directly in spindles will be necessary to determine whether the effects of dynein inhibition on spindle dynamics and morphology can be quantitatively understood in terms of the loss of this contractile stress. Finally, these results more generally shed light on active matter systems far from equilibrium, and show that complex non-equilibrium behaviors can be quantitatively understood in terms of simple phenomenological models.

This chapter details and largely reproduces work previously published as, B Kaye, PJ Foster*, TY Yoo*, DJ Needleman, ”Developing and Testing a Bayesian Analysis of Fluorescence Lifetime Measurements”, PLoS ONE 2017;12(1);e0169337; doi:10.1371/journal.pone.0169337*

A

Bayesian analysis of FLIM data

A.1 Introduction

Förster resonance energy transfer, or FRET, is a fluorescence technique commonly used to access spatial information on length scales smaller than the diffraction limit of light[99]. In standard fluorescence, illuminating light is used to excite a fluorophore into a higher energy state, and the fluorophore subsequently relaxes into its ground state either by emitting a photon or through a non-radiative decay pathway. If another fluorophore is near, typically within ≈ 10 nm, the two fluorophores can interact through dipole-dipole interactions termed FRET. FRET confers an additional decay path where the excited florophore, termed the donor, can transfer its energy to the nearby, unexcited fluorophore, termed the acceptor, which can then release the energy as a photon or through non-radiative decay. As the emission spectra of commonly used donor and acceptor pairs are spectrally distinct, one common method of measuring the average FRET efficiency is to compare the relative intensities collected from the two channels. However, this method has drawbacks including spectral bleed-through and a sensitivity to changes in fluorophore concentration and excitation light intensity[100].

As an alternative to using fluorescence intensity to quantify FRET, fluorescence lifetime imaging microscopy, or FLIM, can be used[101,102,103,104]. FLIM is a general technique that allows changes in a flurophore's local environment to be probed. While use of FLIM is not limited to measuring changes in FRET, it can be used in this context without some of the drawbacks of an intensity based measurement. In time-domain FLIM, a narrow pulse of light is used to excite fluorophores into an excited state. Fluorophores that decay from their excited states can do so by releasing a photon. A subset of the released photons are detected, and for each detected photon, the arrival time is measured relative to the excitation pulse. The amount of time fluorophores spend in their excited state depends on the number of decay paths available. Donor fluorophores are chosen such that when they decay from their excited states, they do so at a constant rate, leading to photon emission time distributions that are exponential with a single characteristic decay time. This characteristic decay time is known as the fluorescence lifetime and is typically on the order of nanosconds. When donor fluorophores are undergoing FRET, they will spend, on average, a shorter amount of time in their excited states, leading to a reduced lifetime and quantum efficiency[105]. In a sample where only a fraction of donor fluorophores are undergoing FRET, the photon emission time distribution will be the sum of two exponentials with different lifetimes. By comparing the amplitudes of these two exponentials, the relative fraction of donors undergoing FRET can be measured. In practice, additional complications are present, including photons collected from spurious background and time delays introduced by the collection system itself. These effects must be accounted for to infer the relative amplitudes and lifetimes of the emitted photon distributions from the measured photon arrival time histograms. Several approaches have been used in order to estimate these parameters, including least-squares fitting[106], rapid lifetime determination[107], phasor methods[108,109,110], and Bayesian approaches[111], each with their own advantages and disadvantages.

Here we utilize and extend the Bayesian approach previously described[111] to take into account biexponential decays and additional experimental factors and we test the performance of our method using experimental data.

A.2 Materials and Methods

A.2.1 Bayesian Framework

Our framework is based on a previously described Bayesian analysis approach for measuring lifetimes from FLIM data[111]. For an introductory overview of Bayesian analysis, we direct the reader to[112]. Bayes' Law states that given a set of data, t, and a set of model parameters θ, then,

$$p(\theta|t) \propto p(t|\theta) \times p(\theta) \tag{A.1}$$

where $p(\theta|t)$, the probability of the model parameters given the measured data, is referred to as the posterior distribution, $p(t|\theta)$ is referred to as the likelihood function, and $p(\theta)$ is referred to as the prior distribution. The aim of Bayesian inference approaches is to find the posterior distribution for the given model and data, and hence what the probability is for each possible set of model parameters θ.

In time-domain FLIM measurements, a narrow laser pulse is used to excite fluorophores in the sample, and the arrival times of photons emitted from the fluorophores are recorded. Fluorophores undergoing FRET will have a shorter florescence lifetime compared with fluorophores not undergoing FRET. When only a fraction of fluorophores in the sample are undergoing FRET, the resulting distribution of photon emission will be a sum of exponentials, where each exponential has a different lifetime, and each exponential is weighted by the number of photons collected from the respective source. In addition, there exists a constant background of photons due to noise in the detector and stray light, taken to be from a uniform distribution. In the following, we consider photons from each of these sources separately and construct the likelihood function as follows,

$$p(t|\theta) = f_S \times p_S(t|f_S, \tau_S) + f_L \times p_L(t|f_L, \tau_L) + f_B \times p_B(t|f_B) \tag{A.2}$$

where t is the arrival time of a photon relative to the excitation pulse, τ_S and τ_L are respectively the short and long fluorescence lifetimes, f_S and f_L are the fractions of photons from the short and long lifetime distributions respectively, f_B is the fraction of photons from the uniform background given by $f_B = (1 - f_S - f_L)$. Here $p_i(t|f_i)$ is the probability of the photon arriving at time t given that the photon originates from fraction f_i.

Equation A.2 represents the likelihood model when time is taken to be continuous. However, in practice, photon arrival times collected with TCSPC are discretized into bins, and this discretization must be taken into account. If the bins are numbered sequentially and of width Δt, such that b_i represents the bin containing photons with arrival time, $(i-1)\Delta t \leq t \leq i\Delta t$, then the likelihood function becomes,

$$p(t|\theta) = \prod_{i=1}^{N} \Big[f_S \times p_S(t \in b_i | f_S, \tau_S) + f_L \times p_L(t \in b_i | f_L, \tau_L) + \\ f_B \times p_B(t \in b_i | f_B) \Big]^{P_i} \tag{A.3}$$

Thus, Eqn. A.3 serves as the discrete form of the likelihood function, Eqn. A.2.

A.2.2 Instrument Response Function

One complexity in experimental TCSPC measurements is that a delay is introduced to photon arrival times, termed the Instrument Response Function (IRF). In order to account for this effect, the IRF was experimentally measured (see FLIM Measurements). The measured IRF is then convolved with the idealized probability density functions for the exponential distributions in order to construct the likelihood function. Taking this effect into account leads to,

$$p_j(t \in b_i | f_j, \tau_j) = p_{em,j}(t \in b_i | f_j, \tau_j) \otimes IRF(t) \tag{A.4}$$

where $p_{em,j}$ is the idealized exponential distribution, taken to be $\propto\ e^{-t/\tau_j}$, where $j \in \{S, L\}$ is an index labeling the exponential distribution and $IRF(t)$ is the experimentally measured instrument response function.

A.2.3 Posterior Distribution

Using Eqn. A.4 in Eqn. A.3 leads to the final form of our likelihood function,

$$
\begin{aligned}
p(t|\theta) = \prod_{i=1}^{N} \Big[& f_S \times p_{em,S}(t \in b_i | f_S, \tau_S) \otimes IRF(t) \\
& + f_L \times p_{em,L}(t \in b_i | f_L, \tau_L) \otimes IRF(t) \\
& + f_B \times p_B(t \in b_i | f_B) \Big]^{P_i}
\end{aligned}
\tag{A.5}
$$

For comparison with experiments using control dyes where the lifetimes of the two molecules are well characterized, we choose a prior distribution such that the distribution is uniform for the fractions in the domain $f_j \in [0,1]$, and τ_S and τ_L are set to the measured values for Coumarin 153 and Erythrosin B respectively. With this choice of prior, Eqn. A.1 becomes,

$$p(\theta|t) \propto p(t|\theta) \tag{A.6}$$

and hence our posterior distribution is proportional to our likelihood function in the constrained parameter space. To build the posterior distribution, parameter space is searched by evaluating the likelihood function on a grid of uniform spacing. Alternatively, parameter space can be searched stochastically using the Markov chain Monte Carlo method, yielding equivalent results.

A.2.4 EFFECTS OF PERIODIC EXCITATION

For a single exponential decay, the probability of measuring a photon at time t, given a decay lifetime, τ, is given by,

$$p_{em}(t|\tau) \propto e^{-\frac{t}{\tau}} \tag{A.7}$$

Where τ is the lifetime of the fluorophore. In practice, many sequential excitation pulses are used, and it's possible that a fluorophore excited by a given pulse doesn't emit a photon until after a future pulse. Taking this effect into account for a single exponential decay leads to[111],

$$p_{em}(t|\tau, T) \propto \sum_{k=0}^{\infty} e^{-\frac{t+kT}{\tau}} \tag{A.8}$$

where T is the excitation pulse period and k is an index counting previous pulses. The sum is a geometric series, which converges to,

$$p_{em}(t|\tau, T) \propto \frac{1}{1 - e^{\frac{-T}{\tau}}} e^{\frac{-t}{\tau}} \tag{A.9}$$

Thus, accounting for periodic excitations leads to a prefactor $\frac{1}{1-e^{\frac{-T}{\tau}}}$, which for a given T and τ is constant. As we treat exponentials from populations with short and long lifetimes separately, this factor can safely be absorbed into the normalization constant, leaving the probability distribution unchanged.

A.2.5 FLIM Measurements

FLIM measurements were carried out on a Nikon Eclipse Ti microscope using two-photon excitation from a Ti:sapphire pulsed laser (Mai-Tai, Spectra-Physics, 865 nm or 950 nm wavelength, 80 MHz repetition rate, $\approx$ 70 fs pulse width), a commercial scanning system (DCS-120, Becker & Hickl), and hybrid detectors (HPM-100-40, Becker & Hickl). The excitation laser was collimated by a telescope assembly to avoid power loss at the XY galvanometric mirror scanner and to fully utilize the numerical aperture of a water-immersion objective (CFI Apo 40x WI, NA 1.25, Nikon). Fluorescence was imaged with a non-descanned detection scheme with a dichroic mirror (705 LP, Semrock) that was used to allow the excitation laser beam to excite the sample while allowing fluorescent light to pass into the detector path. A short-pass filter was used to further block the excitation laser beam (720 SP, Semrock) followed by an emission filter appropriate for Coumarin and Erythrosin B (550/88nm BP, Semrock, or 552/27nm BP, Semrock). A Becker & Hickl Simple-Tau 150 FLIM system was used for time correlated single photon counting[113]. The instrument response function was acquired using second harmonic generation of a urea crystal[113].

For the data shown in Fig 1, the *TAC range* was set to 7×10^{-8} with a *Gain* of 5, corresponding to a 14 ns maximum arrival time. The *TAC offset* was set to 6.27%. The TAC *limit high* and *limit low* were set to 5.88% and 77.25%, respectively, resulting in a 10 ns recording interval. Erythrosin B and Coumarin 153 samples were prepared at 10 mM and 15 mM, respectively. Lifetimes were measured and fixed at values of 3.921 ns and 0.453 ns for Coumarin 153 and Erythrosin B respectively.

For the data shown in Fig 2, the *TAC range* was set to 5×10^{-8} with a *Gain* of 5, corresponding to a 10 ns maximum arrival time. The TAC *limit high* and *limit low* were set to 95.29% and 5.88%, respectively, resulting in a 10 ns recording interval. Illumination intensity was set such that $\approx 2.5 \times 10^5$ photons per second were recorded at the photon detector. Lifetimes were measured and fixed at values of 4.03 ns and 0.48 ns for Coumarin 153 and Erythrosin B respectively.

For the data shown in Fig 3, all settings and parameters were the same as for Fig 1.

A.2.6 *In vivo* FLIM-FRET measurement

U2OS cell line was maintained in Dulbecco's modified Eagle's medium (DMEM, Gibco), supplemented with 10% Fetal Bovine Serum (FBS, Gibco), and 50 IU/mL penicillin and 50 mg/mL streptomycin (Gibco) at 37°C in a humidified atmosphere with 5% CO2. Cells were seeded on a 25-mm diameter, #1.5-thickness, round coverglass coated with poly-D-lysine (GG-25-1.5-pdl, neuVitro). Transient transfection of pCMV-mTurquoise2-GFP plasmid was done with TransIT-2020 (Mirus), and cells were imaged 24 hours later. During imaging, the cells were maintained at 37°C on a custom-built temperature controlled microscope chamber, while covered with 1.5 ml of imaging media and 2 ml of white mineral oil (VWR) to prevent evaporation. The excitation wavelength was 850 nm, and the emission filter was 470/40 (Chroma). The excitation laser power was adjusted to 4 mW. Becker and Hickl SPCM acquisition parameters were set to 10x zoom, 256x256 image pixels, 5 second integration, and 256 ADC resolution.

A.2.7 Software Implementation

All algorithms were implemented in MATLAB. The code used is freely available on Github at https://github.com/bryankaye1/bayesian-analysis-of-fluorescent-lifetime-data. Posterior distributions were generated by evaluating the likelihood function in a grid space of parameter values and were marginalized before estimation of the mode and mean for each parameter.

A.3 Results

In a sample where only a subset of fluorophores are undergoing FRET, photon emission distributions take the form of a biexponential distribution, with some fraction of the distribution consisting of photons from a short-lifetime exponential, another fraction consisting of photons from a long-lifetime exponential, and some fraction coming from a spurrious background distribution. The goal of FLIM analysis is to infer the relative weights of these distributions, along with the lifetimes of the two exponential distributions, from the measured histogram of photon arrival times (Fig A.1A). Here we apply an analysis based on Bayesian inference in order to infer the most likely set of parameters from experimentally measured data. The output of our algorithm is a posterior distribution, which gives the relative probability of measuring a given set of parameters (Fig A.1B). To characterize our approach, we test our analysis in both the low-photon and low-fraction regimes, representing two extremes where data may be collected.

A.3.1 Low-Photon Regime

While the biexponential nature of FLIM histograms is apparent when the histogram is constructed using a large number of photons (Fig A.1A), the histogram's underlying distribution is less obvious when the photon count is low (Fig A.2A). Previous work has estimated the minimum number of photons necessary to achieve a certain accuracy in determining fluorescence lifetimes from TCSPC measurements[114]. In this regime it can be difficult to extract accurate estimates of the fraction of short-lifetime

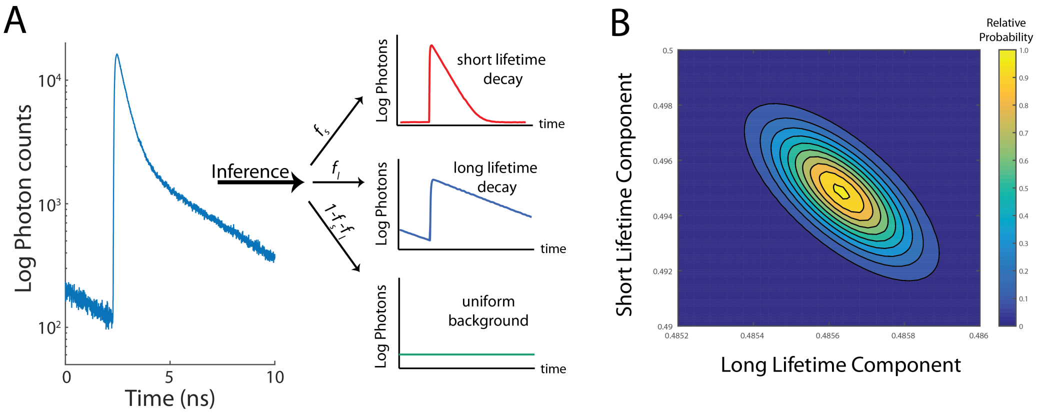

Fig A.1: Photon arrival-time histograms are composed of the sum of two exponential distributions (A) Photon arrival histogram composed of two exponential distributions, with a short-lifetime fraction f_S, a long-lifetime fraction f_L, and a background fraction $f_B = (1 - f_S - f_L)$ (B) Inferred posterior distribution generated from data in Figure A.1A.

photons through methods that rely on histogram fitting. This low-photon regime is relevant in many applications of FLIM, due to the fundamental tradeoff between the number of photons collected and both the spatial-temporal precision of the measurement and the light dose received by the sample. Thus, methods that can improve the precision and accuracy of parameter estimation in the low-photon count regime could potentially lead to a practical increase in spatial-temporal resolution and lower light doses.

In order to test the accuracy and sensitivity of our analysis, fluorescence lifetime measurements were taken using Erythrosin B and Coumarin 153, two reference dyes with well characterized lifetimes of 0.47 ± 0.02 ns and 4.3 ± 0.2 ns respectively[115]. These dyes were mixed at a fixed ratio, and fluorescence lifetime measurements were taken (Fig A.2A, Materials and Methods) in order to generate a master list of photon arrival times. A fixed number of photons were randomly sampled from the master list

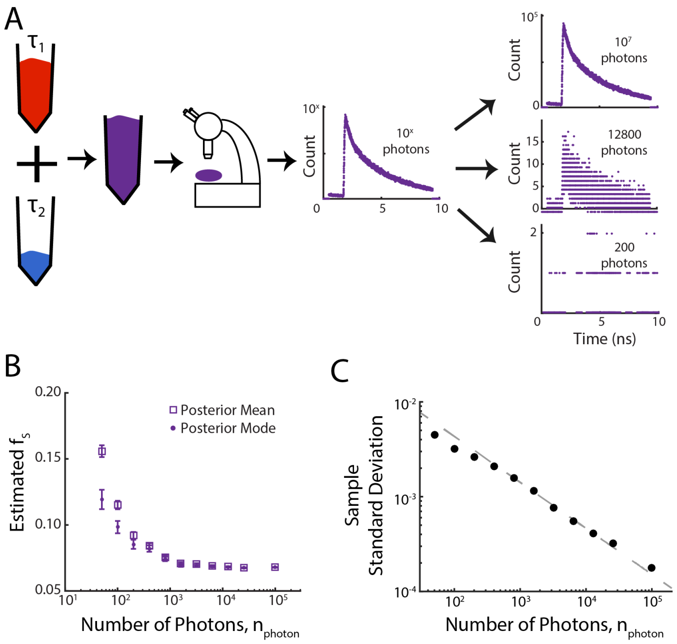

Fig A.2: Low-Photon Regime (A) Control dyes having known long (Coumarin 153) and short (Erythrosin B) lifetimes were mixed at a fixed ratio. From the measured master curve of photon arrival times, a variable number of photons are randomly sampled, generating histograms with a variable number of photons. (B) Bias in the estimated short-life photon fraction, f_S, decreases with increasing photon number. Data points represent the average of the posterior mean (squares) or mode (circles) for 300 independent samplings for each photon count. Error bars are s.e.m. (C) Black circles: measured sample standard deviations from data in Fig A.2B averaged across the 300 independent samplings. The sample standard deviation decreases approximately as $\sqrt{n_{photon}}$. Power law fit to $a \times x^b$ for all but the four lowest values of n_{photon} shown in gray, with $a = 0.04 \pm 0.01$ and $b = -0.48 \pm 0.04$ (95% confidence interval)

in order to construct a histogram of photon arrival times, and analyzed to infer an estimate of the fraction of short-lifetime fluorophores, f_S, taken as either the mean or the mode of the posterior distribution, while the known lifetimes were held fixed (Materials and Methods). This process was repeated 300 times in order to produce an error estimate for each given photon count, and was repeated for total photon counts spanning ≈ 3 orders of magnitude (Fig A.2B).

We find good agreement between the estimates of the fraction of short-lifetime photons for total photons counts larger than ≈ 200 photons, using either the posterior mean or posterior mode as a fraction estimate (Fig A.2B). Slight discrepancies between estimates using the posterior mean and posterior mode are apparent due to truncation and the fact that the posterior distribution is skewed (Fig A.1B), and thus in general the mode and the mean of the distribution are not equal. As a measure of the error in our parameter estimation, we compute the standard deviation of the estimates from the 300 numerical replicates (Fig A.2C) for each photon count. Fitting a power law to all data points except for the four smallest photon counts yields an exponent of -0.48 ± 0.04 (95% confidence interval), consistent with the exponent of -0.5 predicted from the central limit theorem in the limit of high n_{photon} . This $\sqrt{n_{photon}}$ scaling is also evident for other analysis methods, including the rapid lifetime determination method[107], which has comparable error for high n_{photon}.

A.3.2 Low-Fraction Regime

We next tested our results in the regime where a relatively large number of photons are collected, but the fraction of photons originating from the short-lifetime component is low. This regime is relevant in systems where a large number of donor molecules are present, but interactions leading to FRET are relatively rare. In order to test the performance of our algorithm in this regime, fluorescence lifetime measurements were taken of Erythrosin B and Coumarin 153 as representative short- and long-lifetime dyes respectively. Unlike the measurements taken in the low-photon regime, separate fluorescence lifetime measurements were taken for each dye, generating separate master photon histograms (Fig A.3A). A fixed number of photons could then be numerically sampled from each master histogram in order to create test histograms containing a prescribed fraction of photons originating from the short-lifetime dye, which were then analyzed in order to estimate the short-lifetime fraction while the lifetimes were held fixed at their previously measured values (Materials and Methods). Data was collected at $\approx 1.5 \times 10^5$, 1.2×10^6, and 4.8×10^6 counts per second, corresponding to low, medium, and high intensity respectively, and histograms from each intensity were analyzed separately.

Photons were sampled from master curves such that the total number of photons was fixed at 5×10^7, with a prescribed fraction of photons originating from the short-lifetime distribution. This process was repeated 100 times for each condition. Across orders of magnitude, the short-lifetime fraction estimated from our algorithm varies linearly with the prescribed short-lifetime fraction (Fig A.3B), with linear fits giving slopes of 0.9933 ± 0.0026, 1.0085 ± 0.0024, and 1.0106 ± 0.0031, and offsets of $0.002000 \pm 0.0484 \times 10^{-4}$, $0.004400 \pm 0.0814 \times 10^{-4}$, and $0.009500 \pm 0.1992 \times 10^{-4}$ for low, medium, and high intensities respectively (95% confidence interval). The estimated short-lifetime fraction differs from the known short-lifetime fraction by a small bias factor, evident by the small positive offsets in the linear fits (Fig A.3B, Inset). We hypothesize that this offset may be due to a number of factors, including non-monoexponential photon emission from the dyes, slight mischaracterization of the lifetimes or the instrument response function, or an intensity dependence of the FLIM measurement system. While the magnitude of the bias varies with intensity, the magnitude of the bias is relatively small, overestimating the fraction by less than one percent for the highest intensity tested.

In many applications, the changes in FRET fraction are more relevant than the actual fraction values themselves. Thus, we next considered the accuracy of measuring changes in the short-lifetime fraction, which were derived from the results in Fig A.3B by subtracting values adjacent on the short-lifetime fraction axis. While the estimated short-lifetime fractions contain a small bias (Fig A.3B), the bias is largely removed when changes in short-lifetime fraction are considered (Fig A.3C). Consistent with this removal of bias, fitting linear equations to the estimated changes in short lifetime fraction vs. prescribed short lifetime fraction gives slopes of 0.9573 ± 0.1895, 1.0013 ± 0.1445, and 0.9580 ± 0.1717, and offsets of $(0.2332 \pm 0.3712) \times 10^{-5}$, $(0.3215 \pm 0.3088) \times 10^{-5}$, and $(0.4617 \pm 0.4286) \times 10^{-5}$ for low, medium, and high intensities respectively (95% confidence interval) (Fig A.3C). These results demonstrate the accuracy and precision of our method for measuring changes in short-lifetime fraction across many orders of magnitude. For a short-lifetime fraction of 2^{-7}, the sample standard deviation decays with increasing photon number. Fitting a power law yields an exponent of -0.4764 ± 0.0471 (95% confidence interval), consistent with the exponent of -0.5 predicted from the central limit theorem and as was the case for the low-photon regime measurements (Fig A.2C).

A.3.3 *In vivo* TESTING AND METHOD COMPARISON

As FLIM is commonly used to measure FRET in living systems between biological fluorophores, which may contain complications not accounted for in our model, we next tested the applicability of our method in living cells. FLIM measurements were carried out on U2OS cells transfected with a plasmid carrying mTurquoise2-4AA-GFP, a fusion between the FRET pair of mTurquoise2 and GFP (Fig A.4A). As these two fluorophores are physically attached to each other in close proximity, a fraction of the donor mTurquoise2 molecules undergo FRET, and thus have a short lifetime. However, as these fluorophores must undergo maturation before being functional, some fraction of mTurquoise2 molecules will be attached to GFP that are not fully mature and thus will not undergo FRET, leading to a long-lifetime fraction.

To test the performance of our method as a function of the photon number, photon arrival times were pooled within the cell using boxcar windowing, from areas of either 3x3, 7x7, or 11x11 pixels corresponding to average photon counts of 1,087±260, 5,826±1,451, and 14,105±3,673, respectively (Fig A.4B). In order to more readily make comparisons with the least-squares method, we here infer the relative amplitudes of the biexponential decay, instead of the relative photon populations previously considered, and thus consider the long-lifetime amplitude fraction instead of the long-lifetime photon fraction considered above. Using the Bayesian method, the distributions of the long-lifetime fraction were found to have mean and standard deviation values of 0.648±0.069, 0.642±0.037, and 0.640±0.026 (mean ± s.d.) for 3x3, 7x7, and 11x11 binning respectively, showing little change for all conditions.

In order to compare the results from the Bayesian method presented here with the more commonly used least-squares fitting method, we repeated our analysis using fitting routines built into the Becker & Hickl software (Figs A.4A and A.4B). Mean and standard deviation values of the long-lifetime fraction distributions were found to be 0.558±0.137, 0.648±0.050, and 0.652±0.034 (mean ± s.d.) for 3x3, 7x7, and 11x11 binning respectively. While the mean value for the long-lifetime fraction is similar for higher photon counts, there is significant discrepancy for 3x3 binning, where an asymmetric distribution is evident. Furthermore, for the highest photon counts, the mean values agree within error for the Bayesian method and least-squares fitting, indicating a convergence between the two methods in the limit of high photon number. Thus, for low-photon counts, the Bayesian method presented here provides long-lifetime fraction estimates that are more accurate and precise than the nonlinear least-squares method.

A.4 DISCUSSION

Here we presented an extension of previous Bayesian inference approaches to FLIM data analysis that takes into account additional experimental complexities. Using controlled experimental data as a test case, we show that this analysis performs remarkably well in both the low-photon and low-fraction regimes.

In the low-photon regime, we can estimate the low-lifetime fraction, f_S, with a precision of 0.003 and a bias of 0.017 using only 200 photons. At a photon collection rate of 2×10^5 photons per second, this number of photons corresponds to an acquisition time of only 1 millisecond. As the precision scales as $\propto\ n_{photon}^{-1/2}$ (Fig A.2C), if one instead wanted a higher precision of 0.001, one could instead collect data for 9 milliseconds. In the low-fraction regime, using 5×10^7 photons, for a short-lifetime fraction, f_S, of 0.0156, we find a precision of 0.000096 and a bias of 0.0046. With an acquisition rate of 1.5×10^6 photons per second, this corresponds to ≈ 33 seconds of acquisition time. As the precision in this regime also scales $\propto\ n_{photon}^{-1/2}$ (Fig A.3C), if one requires a higher precision of 0.000032, this could be obtained by acquiring data for nine times as long, or 300 seconds. Thus, in both the low-photon and low-fraction regimes, our results show the required number of photons, and hence the acquisition time, necessary to achieve a given level of precision.

One limitation of our implementation is that we evaluate the posterior distribution at equally spaced points. A large parameter space must be searched, and the analysis presented here is relatively slow compared to other parameter searching techniques. For example, when 4 parameters are searched using a Markov chain Monte Carlo approach to stochastically optimize our likelihood, the computation time is reduced by a factor of $\approx$10-20 with no loss of accuracy.

Here we have focused on the use of FLIM to measure changes in FRET, yet it has wider applications, including in metabolic imaging[116] and in measuring local changes in environment, including pH[117] as well as oxygen[118] and Zn^{2+}[119] concentrations. The analysis presented here is general, and should be applicable to FLIM measurements in these other systems as well.

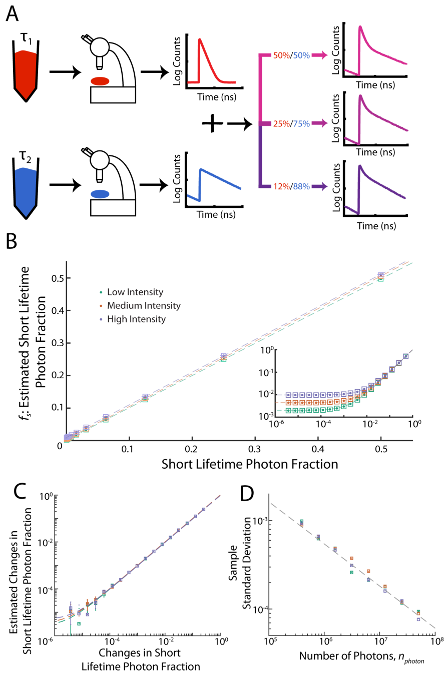

Fig A.3: Low-fraction regime (A) Samples of dyes with short-lifetime (Erythrosin B) and long-lifetime (Coumarin 153) were prepared, and fluorescence lifetime measurements were collected for each dye separately, leading to separate master photon histograms. Test histograms were constructed by randomly sampling a fixed number of photons, with varying fractions being drawn from the master lists of short-lifetime and long-lifetime photons. These histograms were then analyzed in order to estimate the fraction of short-lifetime photons, f_S. (B) The estimated short-lifetime fraction, f_S, varies linearly with the constructed short-lifetime fraction for three different total photon numbers, with a small offset. Squares: estimate from posterior mode. Dots: estimate from posterior mean. Dashed lines: linear fits with slopes 0.9933 ± 0.0026, 1.0085 ± 0.0024, and 1.0106 ± 0.0031, and offsets of $0.002000 \pm 0.0484 \times 10^{-4}$, $0.004400 \pm 0.0814 \times 10^{-4}$, and $0.009500 \pm 0.1992 \times 10^{-4}$ for low, medium, and high intensities respectively (95% confidence interval). Intensities correspond to data collected at $\approx 1.5 \times 10^5$, 1.2×10^6, and 4.8×10^6 counts per second, for low, medium, and high intensity respectively. Inset: Data from main figure shown on a log-log scale. (C) Changes in the estimated short-lifetime fraction track the known changes in the short-lifetime fraction. Squares: estimate from posterior mode. Dots: estimate from posterior mean. Dashed lines: Linear fits with slopes of 0.9573 ± 0.1895, 1.0013 ± 0.1445, and 0.9580 ± 0.1717, and offsets of $(0.2332 \pm 0.3712) \times 10^{-5}$, $(0.3215 \pm 0.3088) \times 10^{-5}$, and $(0.4617 \pm 0.4286) \times 10^{-5}$ for low, medium, and high intensities respectively (95% confidence interval). (D) Sample standard deviations decrease with increasing photon number as $\approx \sqrt{n_{photon}}$ Squares: Posterior standard deviation Dashed line: power law fit to all intensities with exponent -0.4764 ± 0.0471 (95% confidence interval)

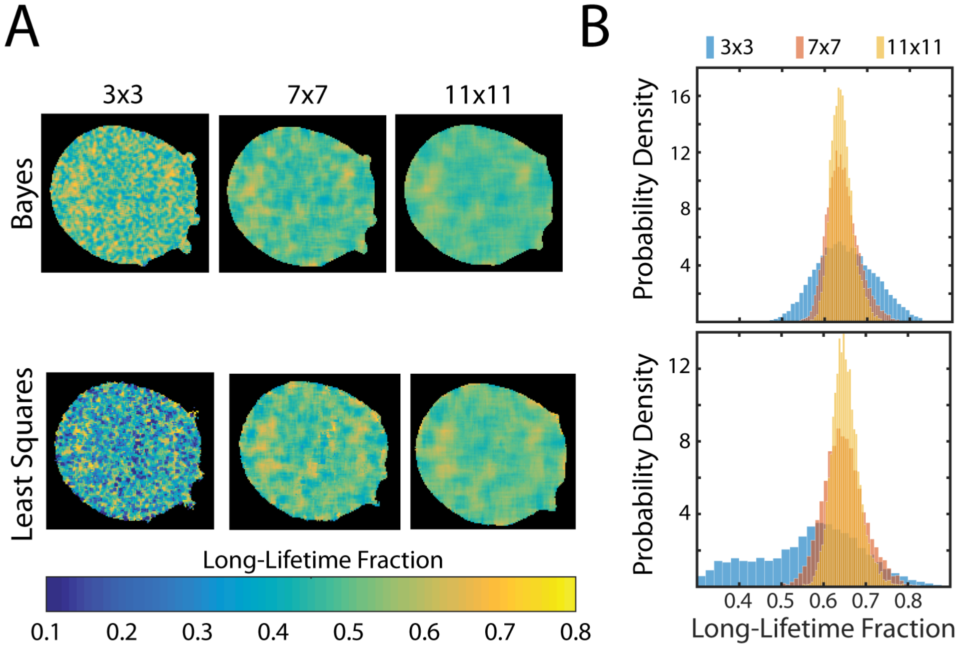

Fig A.4: ***In vivo* Testing** (A) FLIM images depicting the long-lifetime fraction from measurements of mTurquoise2 in a U2OS cell. Photons were pooled from pixels grouped using boxcar windowing into groups of either 3x3, 7x7, or 11x11 pixels and analyzed using either the Bayesian analysis presented here, or least-squares fitting. (B) Histograms showing the probability density of the long-lifetime fraction from images in (A). The probability density functions from Bayesian analysis were found to have mean values of 0.648±0.069, 0.642±0.037, and 0.640±0.026 (mean ± s.d.) for 3x3, 7x7, and 11x11 binning respectively, while the means values were found to be 0.558±0.137, 0.648±0.050, and 0.652±0.034 (mean ± s.d.) for 3x3, 7x7, and 11x11 binning respectively using least-squares-fitting.

This chapter details and largely reproduces work previously published as, PJ Foster, S Fürthauer, MJ Shelley, DJ Needleman, "Active contraction of microtubule networks", eLife 2015;10.7554/eLife.10837 .

B

Active Fluid Model Derivation

We introduce a theoretical description of a confined active microtubule-motor gel immersed in a Newtonian fluid. We obtain generic equations of motion for this system closely following the logic outlined previously[120,121]. This generic description is augmented by including a density-dependent active stress, which is derived from a minimal microscopic description of microtubule-dynein interactions. Here, we present the equations of motion for the one dimensional system.

B.1 Generic theory for an immersed active gel

We begin by stating the conservation laws an active gel permeated by a Newtonian fluid obeys. The system shall be incompressible such that the total density $\rho_{tot} = \rho + \rho_f$ is a constant. Here ρ and ρ_f are the densities of gel and fluid, respectively. The gel density ρ obeys the continuity equation,

$$\partial_t \rho = -\partial_x(\rho v), \tag{B.1}$$

where v is the velocity of the gel. Similarly the fluid permeating the gel obeys,

$$\partial_t \rho_f = -\partial_x(\rho_f v_f), \tag{B.2}$$

where v_f and ρ_f are the fluid density and velocity fields, respectively. Since the overall system is incompressible $\partial_x(\rho v + \rho_f v_f) = 0$. Force balance in the gel requires

$$\partial_x \sigma^{gel} = \bar{\gamma} v + \lambda \left(v - v_f \right), \tag{B.3}$$

where the gel stress $\sigma^{gel} = \eta \partial_x v - \sigma + (\rho/\rho_{tot})P$ consists of a viscous stress $\eta \partial_x v$, an active stress σ, and a hydrostatic pressure P. The friction coefficient $\bar{\gamma}$ quantifies the momentum transfer between the gel and its confinement and λ quantifies the momentum transfer between and the gel and the fluid. The momentum continuity equation of the permeating fluid is

$$0 = \eta_f \partial_x^2 v_f - \partial_x \left[(\rho_f/\rho_{tot})P \right] + \lambda \left(v - v_f \right), \tag{B.4}$$

where η_f is the fluid viscosity. In our experiments, changing the height of the chamber does not appreciably change the time-scale τ of the observed contractions, see Fig. 3F. Furthermore, there is little observed motion of the extract surrounding the film. Presumably $v_f \ll v$ since the system is relatively dilute, i.e. $\rho \ll \rho_f$, and the length-scale $\sqrt{\eta_f/\lambda}$ is large compared to the chamber height. We thus simplify Eq.(B.3) to

$$\eta\partial_x^2 v - \gamma v = \partial_x \sigma, \tag{B.5}$$

where $\gamma = \lambda + \bar{\gamma}$. Eq. (B.5) is the force balance equation we henceforth use for the gel to quantitatively capture the experimental dynamics. Note that $\rho \ll \rho_f$ also allowed us to neglect the hydrostatic pressure in the gel. We complement Eq.(B.5) by the stress boundary condition at the edges of the film at $x = \pm W(t)/2$

$$[\eta\partial_x v - \sigma]_{x=\frac{\pm W(t)}{2}} = 0. \tag{B.6}$$

The width of the film obeys

$$\partial_t W(t) = v\left(W(t)/2\right) - v\left(-W(t)/2\right). \tag{B.7}$$

B.2 Active stresses from dynein-mediated microtubule interactions

We next seek to obtain an expression for the active stress by coarse-graining a microscopic model of interactions between dynein molecular motors and microtubules. Here we assume that dynein builds up near microtubule minus ends as previously suggested[32,122], and hence forces are exchanged between microtubules through the microtubules' minus ends. We introduce the positions of microtubule minus ends x_i, such that the film density can be written as

$$\rho(x) = \sum_i \delta(x - x_i). \tag{B.8}$$

The force exerted by the i-th on the j-th filament is F_{ij}, with $F_{ij} = -F_{ji}$ as required by momentum conservation. The active stress σ generated in this context is defined by the force balance equation

$$\partial_x \sigma = \sum_i \delta(x - x_i) \sum_j F_{ij}, \tag{B.9}$$

up to an arbitrary constant of integration. Note that averaging Eq. (B.9) over an appropriate mesoscopic volume yields the well-known Kirkwood formula. To model microtubule-dynein interactions, we propose that $F_{ij} = A_{ij} + R_{ij}$, where A_{ij} is a dynein-mediated attractive force between minus ends, and R_{ij} is a repulsive force from steric interactions between nearby filaments (Fig. 4). Generically, A_{ij} and R_{ij} depend on the relative positions and orientations of microtubules i and j. Since we are concerned with a disordered assembly of microtubules in which all orientations occur with the same likelihood it is sufficient for our purposes to only think of microtubule positions, and orientation effects average out. The average attractive force A_{ij} that motors bound to the minus end of filament i exert on filament j can be expressed locally as the product

$$A_{ij} = (P_{ij} + P_{ji}) a_{ij}, \tag{B.10}$$

where P_{ij} is the probability that a motor connects the minus end of filament i to filament j and a_{ij} is the force which the motor exerts if a connection is made. Since each dynein can link at most 2 filaments,

$$P_{ij} = m\frac{1 - \Theta(|x_i - x_j| - \Gamma)}{\sum\limits_{k\neq i}(1 - \Theta(|x_i - x_k| - \Gamma))}, \tag{B.11}$$

where m is the fraction of filaments that carry an active motor at their minus end and Γ is a typical interaction distance. Here, $\Theta(x)$ denotes the Heaviside function which is equal to one for positive x and zero otherwise. If a_{ij} is an odd function of the separation vector $x_i - x_j$, it can be expressed by the series $a_{ij} = \sum\limits_{n\geq 1} A_n(x_i - x_j)^{2n-1}$. Using Eq. (B.8), the force density field generated by motor contractions becomes to lowest order in Γ,

$$\sum_i \delta(x - x_i)\sum_j A_{ij} = mA_1\frac{2\Gamma^2}{3}\partial_x\rho + \mathcal{O}(\Gamma^4), \tag{B.12}$$

which corresponds to an active stress contribution $(2/3)mA_1\Gamma^2\rho$.

We next discuss the average steric force that filament i exerts on filament j. Given the force r_{ij} of a collision event we find

$$R_{ij} = m\,(1 - \Theta(|x_i - x_j| - \Gamma))\,r_{ij}. \tag{B.13}$$

Eq. (B.13) is linear in the motor density m, since only filaments that are being actively moved will sterically displace their neighbors. Note that here we chose the typical interaction distance Γ to be the same in Eq. (B.13) and Eq. (B.10) for simplicity. If $r_{ij} = \sum\limits_{n\geq 1} R_n(x_i - x_j)^{2n-1}$ is an odd function of the displacement between the microtubule ends i and j the force density field generated by steric interactions is

$$\sum_i \delta(x - x_i) \sum_j R_{ij} = mR_1 \frac{2\Gamma^3}{3} \rho \partial_x \rho + \mathcal{O}(\Gamma^5), \tag{B.14}$$

which corresponds to an active stress contribution $mR_1\Gamma^3\rho^2/3$. The total active stress is thus given by,

$$\sigma = s\rho(\rho - \rho_0), \tag{B.15}$$

with $s = -mR_1\Gamma^3/3$ and $\rho_0 = -2A_1/(R_1\Gamma)$. Together with Eqns. (B.1,B.5,B.15) are the equations of motions of our system.

B.3 Scaling analysis of the equations of motion

We asked how the characteristic time of contractions scales as a function of the width W_0 of the confining chamber, according to our theory. For this, we rewrite the equations of motion, Eqns. (B.1,B.5), in dimensionless form

$$\delta^2 \partial_{\hat{x}}^2 \hat{v} - \hat{v} = \partial_{\hat{x}}(\hat{\rho}(\hat{\rho} - 1)) \tag{B.16}$$

$$\partial_{\hat{t}} \hat{\rho} = -\partial_{\hat{x}} \hat{\rho} \hat{v} \tag{B.17}$$

where $\hat{x} = x/W_0$, $\hat{v} = vT/W_0$, $\delta = \ell/W_0$, $\ell = \sqrt{\eta/\gamma}$ and $\hat{\rho} = \rho/\rho_0$ and $T = \gamma W_0^2/(s\rho_0^2)$. The boundary condition then becomes

$$\left[\partial_{\hat{x}} \hat{v} - \frac{1}{\delta^2}(\hat{\rho}(\hat{\rho} - 1))\right]_{\hat{x} = \frac{\pm \hat{w}(t)}{2}} = 0 \tag{B.18}$$

with $\hat{w}(t) = W(t)/W_0$. To further simplify our analysis we move to the ”Lagrangian” frame defined by $\chi = \hat{x}/(2\hat{w}(t))$, where the equations of motion become

$$\delta^2 \partial_\chi^2 \hat{v} - \frac{\hat{w}(t)^2}{4}\hat{v} = \frac{\hat{w}(t)}{2}\partial_\chi(\hat{\rho}(\hat{\rho}-1)) \tag{B.19}$$

$$\partial_{\hat{t}}\hat{\rho} = -\frac{2}{\hat{w}(t)}\partial_\chi\left(\hat{\rho}\hat{v} - \frac{\chi\partial_{\hat{t}}\hat{w}(t)}{2}\hat{\rho}\right) - \hat{\rho}\frac{\partial_{\hat{t}}\hat{w}(t)}{\hat{w}(t)} \tag{B.20}$$

with the boundary conditions

$$\left[\partial_\chi \hat{v} - \frac{\hat{w}(t)}{2\delta^2}(\hat{\rho}(\hat{\rho}-1))\right]_{\chi=\pm 1} = 0 \tag{B.21}$$

This system of equations has steady-states for $\hat{\rho} = 1$, $\hat{w}(t) = w$, $\hat{v} = 0$, where w is the final width of the film. We next linearize around this steady state, i.e., choose $\hat{\rho} = 1 + \varepsilon\bar{\rho}$, $\hat{w}(t) = w + \varepsilon\bar{w}$, $\hat{v} = \varepsilon\bar{v}$, where ε is a small quantity. To linear order the equations of motion then become

$$\delta^2\partial_\chi^2\bar{v} - \frac{w^2}{4}\bar{v} = \frac{w}{2}\partial_\chi\bar{\rho} \tag{B.22}$$

$$\partial_{\hat{t}}\bar{\rho} = -\frac{2}{w}\partial_\chi\bar{v} \tag{B.23}$$

and

$$\partial_\chi\bar{v} = \frac{w}{2\delta^2}\bar{\rho} \quad \text{at} \quad \chi \pm 1. \tag{B.24}$$

Using Eqns. (B.22, B.23), we find

$$\left(\delta^2\partial_\chi^2 - \frac{w^2}{4}\right)\partial_{\hat{t}}\bar{\rho} = -\partial_\chi^2\bar{\rho} \tag{B.25}$$

and the boundary condition

$$\partial_{\hat{t}}\bar{\rho} = -\frac{1}{\delta^2}\bar{\rho} \quad \text{at} \quad \chi \pm 1. \tag{B.26}$$

We solve this equation by making the Ansatz $\bar{\rho}(t) = \sum\limits_{k=1}^{\infty}\rho_k(t)\cos\left((2k-1)\frac{\pi}{2}\chi\right) + \rho_0 e^{-t/\delta^2}$, and find

$$A_k\dot{\rho}_k + B_k\rho_k = C_k e^{-t/\delta^2}, \tag{B.27}$$

with $A_k = \left(\delta^2\pi^2(2k-1)^2 + w^2\right)/4$, $B_k = \pi^2(2k{-}1)^2/4$ and $C_k = -\rho_0 w^2(-1)^k/\left(\delta^2\pi(2k-1)\right)$. Thus,

$$\rho_k = \frac{C_k}{B_k/A_k - 1/\delta^2}e^{-t/\delta^2} - K_k e^{-(B_k/A_k)t}, \tag{B.28}$$

where K_k is an integration constant determined from the initial condition. In the following we shall consider the case $\rho_k(t = 0) = 0$, i.e. we start with a uniformly stretched film, for which $K_k = \frac{C_k}{B_k/A_k - 1/\delta^2}$.

To determine the time scale of the width contractions we need to remember the conservation of mass

$$M = \int_{-1}^{1} d\chi \frac{w+\bar{w}}{2}\left(\rho + \bar{\rho}\right) \tag{B.29}$$

which yields

$$\bar{w} = w\int_{-1}^{1} d\chi\bar{\rho}. \tag{B.30}$$

We determine the time-scale τ of contractions from $T/\tau = -\dot{\bar{w}}/\bar{w}$ and find

$$\tau(t) = \frac{\sum\limits_{k=1}^{\infty} K_k \left(e^{-t/\delta^2} - e^{-(B_k/A_k)t}\right) \frac{4(-1)^{k+1}}{\pi(2k-1)} + 2\rho_0 e^{-t/\delta^2}}{\sum\limits_{k=1}^{\infty} K_k \left(e^{-t/\delta^2}/\delta^2 - e^{-(B_k/A_k)t}(B_k/A_k)\right) \frac{4(-1)^{k+1}}{\pi(2k-1)} + \frac{2\rho_0}{\delta^2} e^{-t/\delta^2}}. \tag{B.31}$$

Thus, the dynamics is governed by multiple relaxation processes with varying time-scales. In particular

$$\frac{1}{T} \lim_{t\to 0} \tau(t) = \frac{\delta^2}{(w/2)^2 + 1} \tag{B.32}$$

and

$$\frac{1}{T} \lim_{t\to \infty} \tau(t) = \delta^2 + \frac{w^2}{\pi^2} \tag{B.33}$$

In the experimental parameter regime, the time scale we measure is presumably intermediate,

$$\tau = \alpha \frac{\eta}{s\rho_0^2} + \beta \frac{\gamma}{s\rho_0^2} W_0^2, \tag{B.34}$$

where α and β are dimensionless quantities which we determine numerically. To obtain α and β for a given set of input parameters, we numerically solve Eqns. (B.1,B.5,B.7) and extract the time scale $\tau(W_0)$ for several initial widths. We then fit the results to the functional form of Eq. B.34.

In the experimental regime, using the parameters for which the theoretical contraction profiles best agree with the numerical one (see Fig 5B), we estimate $\alpha \simeq 2.2 \pm 0.05$ and $\beta \simeq 0.085 \pm 0.006$. The error estimates were obtained by sampling α and β over a range of input parameters between half and twice the best fit values, and evaluating a standard error on the computed values.

B.4 NUMERICAL TREATMENT

To solve Eqns. (B.1,B.5,B.7) numerically, we discretize the system by representing ρ on an equispaced grid between $x = -W(t)/2$ and $x = W(t)/2$, where $W(t)$ is the instantaneous width of the contracting film. The instantaneous film velocity is determined from Eq. (B.5) using a second order finite difference scheme. The boundary conditions $\sigma = 0$ at $x = \pm W(t)/2$, are implemented using an asymmetric second order finite difference stencil[123]. We determine the time derivative of density using Eq. (B.20) with the boundary condition specified in Eq. (B.21), which account for the grid contracting with the width of the film. We time-evolve Eqns. (B.20,B.7) using a adaptive second order time stepping provided by Scientific Python project.

C

Materials and Methods

C.1 PREPARATION OF *Xenopus* EXTRACTS

CSF-arrested extracts were prepared from *Xenopus llaevis* oocytes as previously described[124]. Crude extracts were sequentially filtered through 2.0, 1.2, and 0.2 micron filters, frozen in liquid nitrogen, and stored at -80 °C until use.

C.2 PREPARATION OF MICROFLUIDIC DEVICES

Channel negatives were designed using AutoCAD 360 (Autodesk) and Silhouette Studio (Silhouette America) software, cut from 125 micron thick tape (3M Scotchcal) using a Silhouette Cameo die cutter, and a master was made by adhering channel negatives to the bottom of a petri dish. PDMS (Sylgard 184, Dow Corning, 10:1 mixing ratio) was cast onto the masters and cured overnight at 60 °C. Devices and coverslips were each corona treated with air plasma for 1 minute before bonding. Channels containing a degassed solution of 5 mg/mL BSA (J.T. Baker) supplemented with 2.5% w/w Pluronic F127 (Sigma) were incubated overnight at 12 °C. Unless stated otherwise, the microfluidic devices had a length of 18 mm, a height of 0.125 mm, and a width of 1.4 mm.

C.3 Protein Purification

GST-tagged p150-CC1 plasmid was a gift from Thomas Surrey[7]. GST-p150-CC1 was expressed in E. Coli BL21 (DE3)-T1$^{\mathrm{R}}$(Sigma) for 4 hours at 37 °C. The culture was shifted to 18 °C for 1 hour before adding 0.2mM IPTG and the culture was grown overnight at 18 °C. Cells were centrifuged, resuspended in PBS supplemented with Halt Protease Inhibitor Cocktail (Thermo Scientific) and benzonase (Novagen) before lysis by sonication. GST-p150-CC1 was purified from clarified lysate using a GSTrap column FF (G.E. Healthcare) as per the manufacturer's instructions. GST-p150-CC1 was dialyzed overnight into 20mM Tris-HCl, 150mM KCl and 1mM DTT. The GST tag was cleaved using Prescission Protease (overnight incubation at 4 °C). After removing free GST and Prescission Protease using a GSTrap FF column, p150-CC1 was concentrated, frozen in liquid nitrogen, and stored at -80 °C until use.

C.4 Bulk Contraction Assay

20 μL aliquots of filtered extract were supplemented with ~1 μM Alexa-647 labeled tubulin and 2.5μM Taxol before being loaded into channels. For dynein inhibition

experiments, 1 μL of either p150-CC1 or buffer alone was added to the extract immediately before Taxol addition. For Kinesin-5 inhibition experiments, 100 μM STLC (Sigma Aldrich) was added concurrently with Taxol. Channels were sealed with vacuum grease and imaged using a spinning disk confocal microscope (Nikon Ti2000, Yokugawa CSU-X1), an EMCCD camera (Hamamatsu), and a 2x objective using Metamorph acquisition software (Molecular Devices). t=0 is defined when the imaging begins, $\approx$ 1 minute after Taxol addition to the extract. After a brief lag time, the microtubule networks spontaneously begin contraction. Images were analyzed using ImageJ and custom build MATLAB and Python software(available at https://github.com/peterjfoster/eLife). Parameters were fit to contraction data using timepoints where $\epsilon(t) > 0.1$.

C.5 Chapter 2, Final Density Estimation

The final density was estimated using contraction experiments with 2.5 μM Taxol in 0.9 mm channels. For each experiment, the frame closest to t = τ + T_c was isolated, where τ and T_c are the timescale of contraction and the offset time respectively, obtained from fits of the time course of contraction to Eqn. 2 of the main text. After correcting for the camera offset and inhomogeneous laser illumination, the average fluorescence intensity of the network, ρ_N and the average fluorescence intensity in the channel outside the network, ρ_M were calculated. The fluorescence intensity in the channel but outside the network comes from monomeric fluorescently labeled tubulin and was assumed to be constant throughout the channel. The fractional concentration was then estimated as $\rho(\tau + T_c) = \frac{\rho_N - \rho_M}{\rho_N + \rho_M}$. Using this measurement along with the fit curves for ϵ(t) and under the assumption that the network contracts in the z direction such that ϵ(t) in the z direction is the same as along the width, the inferred fractional concentration at t = ∞ was calculated as

$$\rho(t=\infty) = \frac{\rho(\tau + T_c)}{(1-\epsilon_\infty)^2}(1-\epsilon_\infty(1-e^{-1}))^2$$

Assuming the fluorescently labeled tubulin incorporates into microtubules at the same rate as endogenous tubulin, we can multiply the derived fractional density ρ(t = ∞) by the tubulin concentration in extract, 18μM[125] to arrive a final network tubulin concentration of 30 μM.

C.6 Density Profile Measurements

Images from contraction experiments were corrected for the camera offset and inhomogeneous laser illumination before being thresholded in order to segment the microtubule network from background fluorescence. Rotations of the channel relative to the CCD were detected by fitting a linear equations to edges of the microtubule network. If the average of the slopes from the top and bottom of the network was greater than 1/(the number of pixels in the length of the image), a rotated, interpolated frame was constructed where pixels were assigned based on the intensity of the pixel in the original frame weighted by their area fraction in the interpolated pixel. Frames were averaged along the length of the channel before background signal subtraction. For density profiles compared with simulations, the edge peaks of the density profile were identified and pixels between the two peaks were retained. Profiles were normalized such that the integral of the profile was set to 1.

C.7 Particle Imaging Velocimetry

Particle Imaging Velocimetry was performed using PIVLab software[126] using the FFT window deformation algorithm with a 16 pixel interrogation area and 8 pixel step for the first pass and an 8 pixel interrogation area with a 4 pixel step for the second pass. After PIV was performed, intensity images were thresholded to segment the microtubule network from the background, and only velocity vectors within the microtubule network that were $>$ 8 pixels from the network's edges were retained.

C.8 Chapter 3, Initial and final density estimation

In order to estimate network densities, we first assume that Alexa-647 uniformly incorporates into microtubules, and the overall concentration of tubulin is taken to be constant and equal to the previously measured value of 18 μM[125]. From this we can take,

$$18\mu M = \frac{\sum_{i=1}^{N} M_i}{\sum_{i=1}^{N} V_i} = \beta\frac{\sum_{i=1}^{N} I_i a}{\sum_{i=1}^{N} a} = \beta\langle I\rangle_N$$

where M_i is the mass in pixel i, V_i is the volume of pixel i, N is the total number of pixels, beta is a constant conversion factor between units of micromolar and fluorescence intensity, I_i is the measured intensity of pixel i, a is the are of pixel i, and $\langle I\rangle_N$ is the measured intensity averaged over all pixels in the channel. From this we can infer,

$$\beta = \frac{18\mu M}{\langle I\rangle_N}$$

The intensity at each pixel in the network contains a contribution from polymerized tubulin ρ_i and from monomeric, unpolymerized tubulin B. The signal from monomeric tubulin is assumed to be constant and homogeneous throughout the channel. Thus, at the given time point where the background and network intensities are measured, the concentration of polymerized tubulin in the network is given by,

$$\rho_{\mu M}(t) = \frac{\beta}{N_{network}} \sum_{i=1}^{N_{network}} N_i = \frac{\beta}{N_{network}} \sum_{i=1}^{N_{network}} [I_i - B] = \beta[\langle I\rangle_{network} - B] = 18\mu M \frac{\langle I\rangle_{network} - B}{\langle I\rangle_N}$$

where $N_{network}$ is the number of pixels in the network at the time point, and $\langle I\rangle_{network}$ is the intensity averaged over all pixels in the network.

To estimate the network density, the frame closest to t $= T_c + \tau$ was corrected for contributions from dark current and inhomogeneous illumination, and analyzed as above to find $\rho_{\mu M}(T_c + \tau)$. As we assume no microtubules are created, destroyed, or added to the network during the contraction process, the total mass of microtubules in the network must be conserved. Thus,

$$M_{network} = \rho(0)V_0 = \rho(T_c + \tau)V_{T_c+\tau} = \rho_F(\infty)V_F$$

From which,

$$\rho(0) = \rho(T_c + \tau)\frac{V_{T_c+\tau}}{V_0} = \rho(T_c + \tau)\frac{W_{T_c+\tau}H_{T_c+\tau}L_{T_c+\tau}}{W_0 H_0 L_0}$$

We assume that, as the network is pinned at the channel's inlet and outlet, there is no change in volume along the channel's length, and thus $L_0 = L_{T_c+\tau}$. Combining Eqns. 3.1 and 3.2,

$$\epsilon(t = T_c + \tau) = \epsilon_\infty(1 - e^{-1}) = \frac{W_0 - W(t = T_c + \tau)}{W_0} = 1 - \frac{W_{T_c+\tau}}{W_0}$$

Which simplifies to,

$$\frac{W_{T_c+\tau}}{W_0} = 1 - \epsilon_\infty(1 - e^{-1})$$

We further assume that the change in the network's height follows the same functional form as the change in width and thus,

$$\rho(0) = \rho(T_c + \tau)[1 - \epsilon_\infty(1 - e^{-1})]^2$$

For the final density of the network, similar reasoning can be used to show,

$$\rho_F = \frac{1}{(1 - \epsilon_\infty)^2}\rho_0 = \frac{[1 - \epsilon_\infty(1 - e^{-1})]^2}{(1 - \epsilon_\infty)^2}\rho(T_c + \tau)$$

C.9 MEASUREMENT OF MICROTUBULE LENGTH DISTRIBUTIONS

Stabilized microtubules were dissociated from motor proteins and fixed as previously described[70]. Briefly, Alexa-647 labeled tubulin was added to 20 μL *Xenopus* extract at a final concentration of $\approx$1 μM, and 0.5 μL taxol suspended in DMSO was added to the indicated concentration. Microtubules were allowed to assemble at room temperature for 30 minutes unless otherwise noted before 5 μL of extract was diluted into 50 μL of Microtubule Dissociation Buffer (250 mM NaCl, 10 mM K-HEPES, pH 7.7, 1 mM $MgCl_2$, 1 mM EGTA, and 20 μM taxol). After a 2 minute incubation, 100 μL of Fix Buffer (0.1% glutaraldehyde in 60% glycerol, 40% BRB80) was added and incubated for 5 minutes. 1 mL of Dilution Buffer (60% glycerol, 40% BRB80) was then added to dilute the sample, and 2 μL of the diluted sample was spread between a slide and a 22×22 mm^2 coverslip. After waiting 30 minutes to allow the microtubules to adhere to the coverslip, microtubules were imaged using spinning disk confocal microscopy Nikon Ti2000 microscope (Yokugawa CSU-X1 spinning disk, Hamamatsu ImagEM camera, 60x objective, Metamorph acquisition software). Active contours were fit to individual microtubules using the ImageJ plugin JFilament[85], and microtubule lengths were determined from the contours using custom MATLAB software. For each taxol concentration, distributions of microtubule lengths were fit to a log-normal distribution to find the location parameter, μ, and the scale parameter, σ. These parameters were used to determine the mode microtubule length for each distribution using,

$$l_{mode} = e^{\mu - \sigma^2}$$

C.10 XCTK2 End Accumulation Assay

Biotinylated microtubules were attached to treated glass surfaces largely following a previously published protocol[95]. Briefly, slides and coverslips were treated with acetone followed by rinsing with water, ethanol followed by rinsing with water, and potassium hydroxide followed by rinsing with water. Slides and coverslips were dried before silanization in PlusOne Repel-Silane (a 2% solution of dimethyldichlorosilane in octamethylcyclooctasilane). Excess silane was removed with ethanol washes followed by water washes. Flow channels were assembled from treated slides and coverslips using double sided sticky tape as a spacer. The channels were incubated with for 5 minutes with 7.7 mg/mL neutravidin followed by a 30 minute incubation with 5% Pluronic-F127 to passivate the surface. To further passivate the surface, the channels were then incubated for 30 minutes in 10 mg/mL BSA. Taxol stabilized microtubules containing $\approx$ 8% biotin labeled tubulin and $\approx$ 8% Alexa-647 labeled tubulin were diluted 1:200 before a 20 minute incubation in the channel. Reaction buffer consisting of 1x Self-organization Buffer, 20 μM taxol, and 100 nM XCTK2 was then added to the channels, which were then sealed with wax and imaged using a Ti2000 microscope (Yokugawa CSU-X1 spinning disk, Hamamatsu ImagEM camera, 60x objective, μManager acquisition software).

C.11 XCTK2 BULK CONTRACTION

2x Self-Organization Buffer, adapted from a previously described recipe[54], was made containing 40 mM PIPES, 2 mM EGTA, 14.5 mM $MgCl_2$, 10 mM ATP, 3 mM GTP, 2 mM β-ME, 100 mM KCl, 400 mM Sucrose, and 61.2 mM Dextrose. The final reaction mix consisted of 10 μL 2x Self-Organization Buffer, 0.6 μL Gloxy System (to 1x final) 0.5 μL Alexa-647 labeled tubulin (4 μM final), 2.15 μL unlabeled tubulin (36 μM final), 1 μL XCTK2, 0.7 μL PK/LDH, 0.5 μL PEP (26.7 mM final), and 4.15 μL water. Microtubules were assembled by adding 0.4 μL of 100 μM taxol to the mix. The mix was then added to the imaging chamber, either a rectangular microfluidic device as described above, or a 110 μm × 0.9 mm × 18 mm device made by adhering a 100 μm thick PDMS space to a slide and bonding to a coverslip. In either case, the imaging chamber was passivated overnight at 12 °C in a degassed solution of 5 mg/mL BSA supplemented with 2.5% w/w Pluronic F127. After the reaction mix was loaded into the chamber, the chambers were sealed with either vacuum grease for the microfluidic devices, or with wax for the devices with a thin PDMS spacer.

References

[1] J. C. Gatlin, A. Matov, A. C. Groen, D. J. Needleman, T. J. Maresca, G. Danuser, T. J. Mitchison, and E. D. Salmon, "Spindle fusion requires dynein-mediated sliding of oppositely oriented microtubules.," *Current biology : CB*, vol. 19, pp. 287–296, Feb. 2009.

[2] R. Heald, R. Tournebize, T. Blank, R. Sandaltzopoulos, P. Becker, A. Hyman, and E. Karsenti, "Self-organization of microtubules into bipolar spindles around artificial chromosomes in Xenopus egg extracts.," *Nature*, vol. 382, pp. 420–425, Aug. 1996.

[3] K. E. Sawin, K. LeGuellec, M. Philippe, and T. Mitchison, "Mitotic spindle organization by a plus-end-directed microtubule motor.," *Nature*, vol. 359, pp. 540–543, Oct. 1992.

[4] T. Mitchison, P. Maddox, J. Gaetz, A. Groen, M. Shirasu, A. Desai, E. D. Salmon, and T. Kapoor, "Roles of polymerization dynamics, opposed motors, and a tensile element in governing the length of Xenopus extract meiotic spindles.," *Molecular Biology of the Cell*, vol. 16, pp. 3064–3076, June 2005.

[5] A. Merdes, R. Heald, K. Samejima, W. C. Earnshaw, and D. W. Cleveland, "Formation of spindle poles by dynein/dynactin-dependent transport of NuMA.," *The Journal of cell biology*, vol. 149, pp. 851–861, May 2000.

[6] J. Gaetz and T. M. Kapoor, "Dynein/dynactin regulate metaphase spindle length by targeting depolymerizing activities to spindle poles.," *The Journal of cell biology*, vol. 166, pp. 465–471, Aug. 2004.

[7] M. Uteng, C. Hentrich, K. Miura, P. Bieling, and T. Surrey, "Poleward transport of Eg5 by dynein-dynactin in Xenopus laevis egg extract spindles.," *The Journal of cell biology*, vol. 182, pp. 715–726, Aug. 2008.

[8] M. K. Gardner, D. C. Bouck, L. V. Paliulis, J. B. Meehl, E. T. O'Toole, J. Haase, A. Soubry, A. P. Joglekar, M. Winey, E. D. Salmon, K. Bloom, and D. J. Odde, "Chromosome congression by Kinesin-5 motor-mediated disassembly of longer kinetochore microtubules.," *Cell*, vol. 135, pp. 894–906, Nov. 2008.

[9] Y. Chen and W. O. Hancock, "Kinesin-5 is a microtubule polymerase.," *Nature Communications*, vol. 6, p. 8160, 2015.

[10] K. S. Burbank, T. J. Mitchison, and D. S. Fisher, "Slide-and-cluster models for spindle assembly.," *Current Biology*, vol. 17, pp. 1373–1383, Aug. 2007.

[11] A. A. Hyman and E. Karsenti, "Morphogenetic properties of microtubules and mitotic spindle assembly," *Cell*, vol. 84, pp. 401–410, Feb. 1996.

[12] T. Mitchison, P. Maddox, A. Groen, L. Cameron, Z. Perlman, R. Ohi, A. Desai, E. D. Salmon, and T. Kapoor, "Bipolarization and poleward flux correlate during Xenopus extract spindle assembly.," *Molecular Biology of the Cell*, vol. 15, pp. 5603–5615, Dec. 2004.

[13] A. S. Kashina, R. J. Baskin, D. G. Cole, K. P. Wedaman, W. M. Saxton, and J. M. Scholey, "A bipolar kinesin," *Nature*, vol. 379, pp. 270–272, Jan. 1996.

[14] D. J. Sharp, K. McDonald, H. M. Brown, H. J. Matthies, C. Walczak, R. Vale, T. Mitchison, and J. M. Scholey, "The bipolar kinesin, KLP61F, cross-links microtubules within interpolar microtubule bundles of Drosophila embryonic mitotic spindles.," *The Journal of cell biology*, vol. 144, pp. 125–138, Jan. 1999.

[15] L. C. Kapitein, E. J. G. Peterman, B. H. Kwok, J. H. Kim, T. M. Kapoor, and C. F. Schmidt, "The bipolar mitotic kinesin Eg5 moves on both microtubules that it crosslinks.," *Nature*, vol. 435, pp. 114–118, May 2005.

[16] J. Cahu, A. Olichon, C. Hentrich, H. Schek, J. Drinjakovic, C. Zhang, A. Doherty-Kirby, G. Lajoie, and T. Surrey, "Phosphorylation by Cdk1 increases the binding of Eg5 to microtubules in vitro and in Xenopus egg extract spindles.," *PloS one*, vol. 3, no. 12, p. e3936, 2008.

[17] N. P. Ferenz, R. Paul, C. Fagerstrom, A. Mogilner, and P. Wadsworth, "Dynein antagonizes eg5 by crosslinking and sliding antiparallel microtubules.," *Current biology : CB*, vol. 19, pp. 1833–1838, Nov. 2009.

[18] L. Haren and A. Merdes, “Direct binding of NuMA to tubulin is mediated by a novel sequence motif in the tail domain that bundles and stabilizes microtubules.,” *Journal of Cell Science*, vol. 115, pp. 1815–1824, May 2002.

[19] M. E. Tanenbaum, R. Vale, and R. J. McKenney, “Cytoplasmic dynein crosslinks and slides anti-parallel microtubules using its two motor domains,” *eLife*, vol. 2, pp. e00943–e00943, Jan. 2013.

[20] S. Reck-Peterson, R. Vale, and A. Gennerich, “Motile Properties of Cytoplasmic Dynein.” Pan Stanford Publishing, 2012.

[21] J. S. Waitzman and S. E. Rice, “Mechanism and regulation of kinesin-5, an essential motor for the mitotic spindle.,” *Biology of the cell / under the auspices of the European Cell Biology Organization*, vol. 106, pp. 1–12, Jan. 2014.

[22] S. L. Reck-Peterson, A. Yildiz, A. P. Carter, A. Gennerich, N. Zhang, and R. D. Vale, “Single-molecule analysis of dynein processivity and stepping behavior.,” *Cell*, vol. 126, pp. 335–348, July 2006.

[23] R. J. McKenney, W. Huynh, M. E. Tanenbaum, G. Bhabha, and R. D. Vale, “Activation of cytoplasmic dynein motility by dynactin-cargo adapter complexes.,” *Science*, vol. 345, pp. 337–341, July 2014.

[24] M. A. Olenick, M. Tokito, M. Boczkowska, R. Dominguez, and E. L. F. Holzbaur, “Hook Adaptors Induce Unidirectional Processive Motility by Enhancing the Dynein-Dynactin Interaction,” *Journal of Biological Chemistry*, vol. 291, pp. 18239–18251, Aug. 2016.

[25] J. Huang, A. J. Roberts, A. E. Leschziner, and S. L. Reck-Peterson, “Lis1 acts as a ”clutch” between the ATPase and microtubule-binding domains of the dynein motor.,” *Cell*, vol. 150, pp. 975–986, Aug. 2012.

[26] B. H. Kwok, L. C. Kapitein, J. H. Kim, E. J. G. Peterman, C. F. Schmidt, and T. M. Kapoor, “Allosteric inhibition of kinesin-5 modulates its processive directional motility.,” *Nature Chemical Biology*, vol. 2, pp. 480–485, Sept. 2006.

[27] L. C. Kapitein, B. H. Kwok, J. S. Weinger, C. F. Schmidt, T. M. Kapoor, and E. J. G. Peterman, “Microtubule cross-linking triggers the directional motility of kinesin-5,” *The Journal of cell biology*, vol. 182, pp. 421–428, Aug. 2008.

[28] C. Leduc, K. Padberg-Gehle, V. Varga, D. Helbing, S. Diez, and J. Howard, "Molecular crowding creates traffic jams of kinesin motors on microtubules.," *Proceedings Of The National Academy Of Sciences Of The United States Of America*, vol. 109, pp. 6100–6105, Apr. 2012.

[29] F. Verde, J. Berrez, C. Antony, and E. Karsenti, "Taxol-induced microtubule asters in mitotic extracts of Xenopus eggs: requirement for phosphorylated factors and cytoplasmic dynein.," *The Journal of cell biology*, vol. 112, pp. 1177–1187, Mar. 1991.

[30] P. J. Foster, S. Fürthauer, M. J. Shelley, and D. J. Needleman, "Active contraction of microtubule networks.," *eLife*, vol. 4, p. 591, 2015.

[31] A. Khodjakov, L. Copenagle, M. B. Gordon, D. A. Compton, and T. M. Kapoor, "Minus-end capture of preformed kinetochore fibers contributes to spindle morphogenesis.," *The Journal of cell biology*, vol. 160, pp. 671–683, Mar. 2003.

[32] M. W. Elting, C. L. Hueschen, D. B. Udy, and S. Dumont, "Force on spindle microtubule minus ends moves chromosomes," *The Journal of cell biology*, vol. 206, pp. 245–256, July 2014.

[33] G. Fink, L. Hajdo, K. J. Skowronek, C. Reuther, A. A. Kasprzak, and S. Diez, "The mitotic kinesin-14 Ncd drives directional microtubule–microtubule sliding," *Nature Cell Biology*, vol. 11, pp. 717–723, May 2009.

[34] K. T. Vaughan, S. H. Tynan, N. E. Faulkner, C. J. Echeverri, and R. B. Vallee, "Colocalization of cytoplasmic dynein with dynactin and CLIP-170 at microtubule distal ends.," *Journal of Cell Science*, vol. 112 (Pt 10), pp. 1437–1447, May 1999.

[35] A. J. Roberts, B. S. Goodman, and S. L. Reck-Peterson, "Reconstitution of dynein transport to the microtubule plus end by kinesin.," *eLife*, vol. 3, p. e02641, 2014.

[36] J. K. Moore, M. D. Stuchell-Brereton, and J. A. Cooper, "Function of dynein in budding yeast: mitotic spindle positioning in a polarized cell.," *Cell Motility*, vol. 66, pp. 546–555, Aug. 2009.

[37] K. Kruse and F. Julicher, "Actively contracting bundles of polar filaments.," *Physical Review Letters*, vol. 85, pp. 1778–1781, Aug. 2000.

[38] T. B. Liverpool and M. C. Marchetti, "Bridging the microscopic and the hydrodynamic in active filament solutions," *Europhysics Letters (EPL)*, vol. 69, no. 5, pp. 846–852, 2005.

[39] I. Aranson and L. Tsimring, "Theory of self-assembly of microtubules and motors," *Physical Review E*, vol. 74, Sept. 2006.

[40] M. C. Marchetti, J. F. Joanny, S. Ramaswamy, T. B. Liverpool, J. Prost, M. Rao, and R. A. Simha, "Hydrodynamics of soft active matter," *Reviews Of Modern Physics*, vol. 85, pp. 1143–1189, July 2013.

[41] T. Gao, R. Blackwell, M. A. Glaser, M. D. Betterton, and M. J. Shelley, "Multiscale Polar Theory of Microtubule and Motor-Protein Assemblies," *Physical Review Letters*, vol. 114, p. 048101, Jan. 2015.

[42] A. Ahmadi, M. C. Marchetti, and T. B. Liverpool, "Hydrodynamics of isotropic and liquid crystalline active polymer solutions.," *Physical review. E, Statistical, nonlinear, and soft matter physics*, vol. 74, p. 061913, Dec. 2006.

[43] A. Ward, F. Hilitski, W. Schwenger, D. Welch, A. W. C. Lau, V. Vitelli, L. Mahadevan, and Z. Dogic, "Solid friction between soft filaments.," *Nature Materials*, vol. 14, pp. 583–588, June 2015.

[44] F. Hilitski, A. R. Ward, L. Cajamarca, M. F. Hagan, G. M. Grason, and Z. Dogic, "Measuring Cohesion between Macromolecular Filaments One Pair at a Time: Depletion-Induced Microtubule Bundling," *Physical Review Letters*, vol. 114, pp. 138102–6, Apr. 2015.

[45] F. Nédélec and T. Surrey, "Dynamics of microtubule aster formation by motor complexes," *Comptes Rendus de l'Académie des Sciences - Series IV - Physics-Astrophysics*, vol. 2, no. 6, pp. 841–847, 2001.

[46] K. Kruse and F. Jülicher, "Self-organization and mechanical properties of active filament bundles," *Physical Review E*, vol. 67, p. 051913, May 2003.

[47] Y. Shimamoto, S. Forth, and T. M. Kapoor, “Measuring Pushing and Braking Forces Generated by Ensembles of Kinesin-5 Crosslinking Two Microtubules,” *Developmental Cell*, vol. 34, pp. 669–681, Sept. 2015.

[48] S. M. J. L. van den Wildenberg, L. Tao, L. C. Kapitein, C. F. Schmidt, J. M. Scholey, and E. J. G. Peterman, “The homotetrameric kinesin-5 KLP61F preferentially crosslinks microtubules into antiparallel orientations.,” *Current biology : CB*, vol. 18, pp. 1860–1864, Dec. 2008.

[49] A. Hunt and J. Howard, “Kinesin swivels to permit microtubule movement in any direction.,” *Proceedings of the National Academy of Sciences*, vol. 90, pp. 11653–11657, Dec. 1993.

[50] W. Hua, J. Chung, and J. Gelles, “Distinguishing inchworm and hand-over-hand processive kinesin movement by neck rotation measurements.,” *Science*, vol. 295, pp. 844–848, Feb. 2002.

[51] B. Gutiérrez-Medina, A. N. Fehr, and S. M. Block, “Direct measurements of kinesin torsional properties reveal flexible domains and occasional stalk reversals during stepping.,” *Proceedings Of The National Academy Of Sciences Of The United States Of America*, vol. 106, pp. 17007–17012, Oct. 2009.

[52] H. Wald, “Cytologic Studies on the Abnormal Development of the Eggs of the Claret Mutant Type of Drosophila Simulans.,” *Genetics*, vol. 21, pp. 264–281, May 1936.

[53] M. Hatsumi and S. A. Endow, “The Drosophila ncd microtubule motor protein is spindle-associated in meiotic and mitotic cells.,” *Journal of Cell Science*, vol. 103 (Pt 4), pp. 1013–1020, Dec. 1992.

[54] C. Hentrich and T. Surrey, “Microtubule organization by the antagonistic mitotic motors kinesin-5 and kinesin-14,” *The Journal of cell biology*, vol. 189, pp. 465–480, May 2010.

[55] R. Suzuki, C. A. Weber, E. Frey, and A. R. Bausch, “Polar pattern formation in driven filament systems requires non-binary particle collisions,” *Nature Physics*, vol. 11, pp. 839–843, Aug. 2015.

[56] J. Prost, F. Julicher, and J. F. Joanny, “Active gel physics,” *Nature Physics*, vol. 11, pp. 111–117, Feb. 2015.

[57] R. A. Simha and S. Ramaswamy, “Hydrodynamic fluctuations and instabilities in ordered suspensions of self-propelled particles.,” *Physical Review Letters*, vol. 89, p. 058101, July 2002.

[58] M. Wühr, Y. Chen, S. Dumont, A. C. Groen, D. J. Needleman, A. Salic, and T. J. Mitchison, “Evidence for an upper limit to mitotic spindle length.,” *Current Biology*, vol. 18, pp. 1256–1261, Aug. 2008.

[59] M. E. Crowder, M. Strzelecka, J. D. Wilbur, M. C. Good, G. von Dassow, and R. Heald, “A Comparative Analysis of Spindle Morphometrics across Metazoans,” *Current Biology*, vol. 25, pp. 1542–1550, June 2015.

[60] J. Brugues and D. Needleman, “Physical basis of spindle self-organization.,” *Proceedings Of The National Academy Of Sciences Of The United States Of America*, vol. 111, pp. 18496–18500, Dec. 2014.

[61] T. B. Liverpool and M. C. Marchetti, *Hydrodynamics and Rheology of Active Polar Filaments*, pp. 177–206. New York, NY: Springer New York, 2008.

[62] T. Sanchez, D. T. N. Chen, S. J. DeCamp, M. Heymann, and Z. Dogic, “Spontaneous motion in hierarchically assembled active matter.,” *Nature*, vol. 491, pp. 431–434, Nov. 2012.

[63] F. C. Keber, E. Loiseau, T. Sanchez, S. J. DeCamp, L. Giomi, M. J. Bowick, M. C. Marchetti, Z. Dogic, and A. R. Bausch, “Topology and dynamics of active nematic vesicles,” *Science*, vol. 345, pp. 1135–1139, Sept. 2014.

[64] L. Giomi, M. J. Bowick, X. Ma, and M. C. Marchetti, “Defect annihilation and proliferation in active nematics.,” *Physical Review Letters*, vol. 110, p. 228101, May 2013.

[65] J. C. Gatlin, A. Matov, G. Danuser, T. Mitchison, and E. D. Salmon, “Directly probing the mechanical properties of the spindle and its matrix,” *The Journal of cell biology*, vol. 188, pp. 481–489, Feb. 2010.

[66] D. T. Miyamoto, Z. E. Perlman, K. S. Burbank, A. C. Groen, and T. J. Mitchison, “The kinesin Eg5 drives poleward microtubule flux in Xenopus laevis egg extract spindles.,” *The Journal of cell biology*, vol. 167, pp. 813–818, Dec. 2004.

[67] J. Brugués, V. Nuzzo, E. Mazur, and D. J. Needleman, “Nucleation and Transport Organize Microtubules in Metaphase Spindles,” *Cell*, vol. 149, pp. 554–564, Apr. 2012.

[68] B. Wickstead and K. Gull, “A ”holistic” kinesin phylogeny reveals new kinesin families and predicts protein functions.,” *Molecular Biology of the Cell*, vol. 17, pp. 1734–1743, Apr. 2006.

[69] B. Wickstead and K. Gull, “Dyneins across eukaryotes: a comparative genomic analysis.,” *Traffic (Copenhagen, Denmark)*, vol. 8, pp. 1708–1721, Dec. 2007.

[70] T. J. Mitchison, P. Nguyen, M. Coughlin, and A. C. Groen, “Self-organization of stabilized microtubules by both spindle and midzone mechanisms in Xenopus egg cytosol.,” *Molecular Biology of the Cell*, vol. 24, pp. 1559–1573, May 2013.

[71] T. Gaglio, A. Saredi, and D. A. Compton, “NuMA is required for the organization of microtubules into aster-like mitotic arrays.,” *The Journal of cell biology*, vol. 131, pp. 693–708, Nov. 1995.

[72] P. M. Bendix, G. H. Koenderink, D. Cuvelier, Z. Dogic, B. N. Koeleman, W. M. Brieher, C. M. Field, L. Mahadevan, and D. A. Weitz, “A Quantitative Analysis of Contractility in Active Cytoskeletal Protein Networks,” *Biophysical Journal*, vol. 94, pp. 3126–3136, Apr. 2008.

[73] P. Oswald, *Rheophysics : the deformation and flow of matter.* Cambridge: Cambridge University Press, 2014.

[74] O. Coussy, *Poromechanics.* Chichester: Wiley, 2004.

[75] D. J. Needleman, A. Groen, R. Ohi, T. Maresca, L. Mirny, and T. Mitchison, “Fast microtubule dynamics in meiotic spindles measured by single molecule imaging: evidence that the spindle environment does not stabilize microtubules.,” *Molecular Biology of the Cell*, vol. 21, pp. 323–333, Jan. 2010.

[76] Y. Shimamoto, Y. T. Maeda, S. Ishiwata, A. J. Libchaber, and T. M. Kapoor, "Insights into the micromechanical properties of the metaphase spindle.," *Cell*, vol. 145, pp. 1062–1074, June 2011.

[77] M. P. Nicholas, P. Höök, S. Brenner, C. L. Wynne, R. B. Vallee, and A. Gennerich, "Control of cytoplasmic dynein force production and processivity by its C-terminal domain.," *Nature Communications*, vol. 6, p. 6206, 2015.

[78] V. Mountain, C. Simerly, L. Howard, A. Ando, G. Schatten, and D. A. Compton, "The kinesin-related protein, HSET, opposes the activity of Eg5 and cross-links microtubules in the mammalian mitotic spindle.," *The Journal of cell biology*, vol. 147, pp. 351–366, Oct. 1999.

[79] G. Goshima, F. Nédélec, and R. Vale, "Mechanisms for focusing mitotic spindle poles by minus end–directed motor proteins," *The Journal of cell biology*, vol. 171, no. 2, pp. 229–240, 2005.

[80] J. C. Gatlin, A. Matov, G. Danuser, T. J. Mitchison, and E. D. Salmon, "Directly probing the mechanical properties of the spindle and its matrix.," *The Journal of cell biology*, vol. 188, pp. 481–489, Feb. 2010.

[81] I. Linsmeier, S. Banerjee, P. W. Oakes, W. Jung, T. Kim, and M. P. Murrell, "Disordered actomyosin networks are sufficient to produce cooperative and telescopic contractility," *Nature Communications*, vol. 7, pp. 1–9, Aug. 2016.

[82] S. R. Naganathan, S. Fürthauer, M. Nishikawa, F. Jülicher, S. W. Grill, and J. Ferrell, "Active torque generation by the actomyosin cell cortex drives left–right symmetry breaking," *eLife*, vol. 3, p. e04165, Dec. 2014.

[83] M. Mayer, M. Depken, J. S. Bois, F. Jülicher, and S. W. Grill, "Anisotropies in cortical tension reveal the physical basis of polarizing cortical flows," *Nature*, vol. 467, pp. 617–621, Sept. 2010.

[84] N. Kumar, "Taxol-induced polymerization of purified tubulin. Mechanism of action.," *Journal of Biological Chemistry*, vol. 256, no. 20, pp. 10435–10441, 1981.

[85] M. B. Smith, H. Li, T. Shen, X. Huang, E. Yusuf, and D. Vavylonis, “Segmentation and tracking of cytoskeletal filaments using open active contours.,” *Cytoskeleton (Hoboken, N.J.)*, vol. 67, pp. 693–705, Nov. 2010.

[86] C. P. Broedersz, M. Sheinman, and F. MacKintosh, “Filament-length-controlled elasticity in 3D fiber networks.,” *Physical Review Letters*, vol. 108, p. 078102, Feb. 2012.

[87] K. E. Kasza, C. P. Broedersz, G. Koenderink, Y. Lin, W. Messner, E. A. Millman, F. Nakamura, T. P. Stossel, F. MacKintosh, and D. A. Weitz, “Actin Filament Length Tunes Elasticity of Flexibly Cross-Linked Actin Networks,” *Biophysical Journal*, vol. 99, pp. 1091–1100, Aug. 2010.

[88] T. A. Schroer, “DYNACTIN,” *Annual Review of Cell and Developmental Biology*, vol. 20, no. 1, pp. 759–779, 2004.

[89] F. Nédélec, T. Surrey, A. Maggs, and S. Leibler, “Self-organization of microtubules and motors.,” *Nature*, vol. 389, pp. 305–308, Sept. 1997.

[90] T. Torisawa, D. Taniguchi, S. Ishihara, and K. Oiwa, “Spontaneous Formation of a Globally Connected Contractile Network in a Microtubule-Motor System,” *Biophysj*, vol. 111, pp. 373–385, July 2016.

[91] C. E. Walczak, S. Verma, and T. Mitchison, “XCTK2: a kinesin-related protein that promotes mitotic spindle assembly in Xenopus laevis egg extracts.,” *The Journal of cell biology*, vol. 136, pp. 859–870, Feb. 1997.

[92] M. Braun, D. R. Drummond, R. A. Cross, and A. D. McAinsh, “The kinesin-14 Klp2 organizes microtubules into parallel bundles by an ATP-dependent sorting mechanism,” *Nature Cell Biology*, vol. 11, pp. 724–730, May 2009.

[93] H. J. Matthies, H. B. McDonald, L. S. Goldstein, and W. E. Theurkauf, “Anastral meiotic spindle morphogenesis: role of the non-claret disjunctional kinesin-like protein.,” *The Journal of cell biology*, vol. 134, pp. 455–464, July 1996.

[94] X. Su, H. Arellano-Santoyo, D. Portran, J. Gaillard, M. Vantard, M. Thery, and D. Pellman, “Microtubule-sliding activity of a kinesin-8 promotes spindle assembly and spindle-length control.,” *Nature Cell Biology*, vol. 15, pp. 948–957, Aug. 2013.

[95] R. Dixit and J. Ross, "Studying plus-end tracking at single molecule resolution using TIRF microscopy," *Methods in cell biology*, vol. 95, pp. 543–554, 2010.

[96] R. Oldenbourg, "Analysis of microtubule dynamics by polarized light.," *Methods in molecular medicine*, vol. 137, pp. 111–123, 2007.

[97] E. Barry, Z. Dogic, R. B. Meyer, R. A. Pelcovits, and R. Oldenbourg, "Direct measurement of the twist penetration length in a single smectic A layer of colloidal virus particles.," *Journal Of Physical Chemistry B*, vol. 113, pp. 3910–3913, Mar. 2009.

[98] C.-H. Yu, N. Langowitz, H.-Y. Wu, R. Farhadifar, J. Brugués, T. Y. Yoo, and D. Needleman, "Measuring microtubule polarity in spindles with second-harmonic generation.," *Biophysical Journal*, vol. 106, pp. 1578–1587, Apr. 2014.

[99] R. Roy, S. Hohng, and T. Ha, "A practical guide to single-molecule FRET," *NATURE METHODS*, vol. 5, no. 6, pp. 507–516, 2008.

[100] H. Wallrabe and A. Periasamy, "Imaging protein molecules using FRET and FLIM microscopy," *Current opinion in biotechnology*, vol. 16, pp. 19–27, Feb. 2005.

[101] J. C. Stachowiak, E. M. Schmid, C. J. Ryan, H. S. Ann, D. Y. Sasaki, M. B. Sherman, P. L. Geissler, D. A. Fletcher, and C. C. Hayden, "Membrane bending by protein–protein crowding," *Nature Cell Biology*, vol. 14, pp. 944–949, Aug. 2012.

[102] M. Peter, S. M. Ameer-Beg, M. K. Y. Hughes, M. D. Keppler, S. Prag, M. Marsh, B. Vojnovic, and T. Ng, "Multiphoton-FLIM quantification of the EGFP-mRFP1 FRET pair for localization of membrane receptor-kinase interactions.," *Biophysical Journal*, vol. 88, pp. 1224–1237, Feb. 2005.

[103] T. Y. Yoo and D. J. Needleman, "Studying Kinetochores In Vivo Using FLIM-FRET," in *The Mitotic Spindle*, pp. 169–186, New York, NY: Springer New York, May 2016.

[104] E. Hinde, M. A. Digman, and K. M. Hahn, "Millisecond spatiotemporal dynamics of FRET biosensors by the pair correlation function and the phasor approach to FLIM," in *Proceedings of the …*, pp. 135–140, 2013.

[105] J. Lakowicz, *Principles of Fluorescence Spectroscopy.* Springer Science Business Media, 3rd ed., 2006.

[106] C. Chang, D. Sud, and M. A. Mycek, "Fluorescence Lifetime Imaging Microscopy," *Methods in cell biology*, vol. 81, pp. 495–524, 2007.

[107] K. K. Sharman, A. Periasamy, H. Ashworth, and J. N. Demas, "Error analysis of the rapid lifetime determination method for double-exponential decays and new windowing schemes.," *Analytical Chemistry*, vol. 71, pp. 947–952, Mar. 1999.

[108] C. Stringari, A. Cinquin, and O. Cinquin, "Phasor approach to fluorescence lifetime microscopy distinguishes different metabolic states of germ cells in a live tissue," in *Proceedings of the …*, pp. 13582–13587, 2011.

[109] R. A. Colyer, O. H. W. Siegmund, A. S. Tremsin, J. V. Vallerga, S. Weiss, and X. Michalet, "Phasor imaging with a widefield photon-counting detector," *Journal of Biomedical Optics*, vol. 17, no. 1, p. 016008, 2012.

[110] W. Chen, E. Avezov, S. C. Schlachter, F. Gielen, R. F. Laine, H. P. Harding, F. Hollfelder, D. Ron, and C. F. Kaminski, "A method to quantify FRET stoichiometry with phasor plot analysis and acceptor lifetime ingrowth.," *Biophysical Journal*, vol. 108, p. 1002, Mar. 2015.

[111] M. Rowley, P. Barber, A. Coolen, and B. Vojnovic, "Bayesian analysis of fluorescence lifetime imaging data," *Proc. of SPIE Vol*, vol. 7903, pp. 790325–790321, 2011.

[112] D. S. Sivia and J. Skilling, *Data Analysis: A Bayesian Tutorial (Oxford science publications).* Oxford University Press, 2006.

[113] B. W, *The bh TCSPC Handbook.* Becker & Hickl GmbH, 2010.

[114] M. Köllner and J. Wolfrum, "How many photons are necessary for fluorescence-lifetime measurements?," *Chemical Physics Letters*, vol. 200, no. 1-2, pp. 199–204, 1992.

[115] N. Boens, W. Qin, N. Basarić, J. Hofkens, M. Ameloot, J. Pouget, J.-P. Lefèvre, B. Valeur, E. Gratton, M. vandeVen, N. D. Silva, Y. Engelborghs, K. Willaert,

A. Sillen, G. Rumbles, D. Phillips, A. J. W. G. Visser, A. van Hoek, J. R. Lakowicz, H. Malak, I. Gryczynski, A. G. Szabo, D. T. Krajcarski, N. Tamai, and A. Miura, “Fluorescence Lifetime Standards for Time and Frequency Domain Fluorescence Spectroscopy,” *Analytical Chemistry*, vol. 79, pp. 2137–2149, Mar. 2007.

[116] D. K. Bird, L. Yan, K. M. Vrotsos, K. W. Eliceiri, E. M. Vaughan, P. J. Keely, J. G. White, and N. Ramanujam, “Metabolic mapping of MCF10A human breast cells via multiphoton fluorescence lifetime imaging of the coenzyme NADH.,” *Cancer Research*, vol. 65, pp. 8766–8773, Oct. 2005.

[117] H.-J. Lin, P. Herman, and J. R. Lakowicz, “Fluorescence lifetime-resolved pH imaging of living cells,” *Cytometry*, vol. 52A, pp. 77–89, Mar. 2003.

[118] H. C. Gerritsen, R. Sanders, A. Draaijer, and C. Ince, “Fluorescence lifetime imaging of oxygen in living cells,” *Journal of …*, vol. 7, no. 1, pp. 11–15, 1997.

[119] C. Ripoll, M. Martin, M. Roldan, E. M. Talavera, A. Orte, and M. J. Ruedas-Rama, “Intracellular Zn(2+) detection with quantum dot-based FLIM nanosensors.,” *Chemical Communications*, vol. 51, pp. 16964–16967, Dec. 2015.

[120] M. Doi and A. Onuki, “Dynamic coupling between stress and composition in polymer solutions and blends,” *Journal de Physique II*, 1992.

[121] J. F. Joanny, F. Julicher, K. Kruse, and J. Prost, “Hydrodynamic theory for multi-component active polar gels,” *New Journal of Physics*, vol. 9, pp. 422–422, Nov. 2007.

[122] T. Surrey, “Physical Properties Determining Self-Organization of Motors and Microtubules,” *Science*, vol. 292, pp. 1167–1171, May 2001.

[123] A. K. Tornberg and M. Shelley, “Simulating the dynamics and interactions of flexible fibers in Stokes flows,” *Journal of Computational Physics*, vol. 196, no. 1, pp. 8–40, 2004.

[124] E. Hannak and R. Heald, “Investigating mitotic spindle assembly and function in vitro using Xenopus laevis egg extracts,” *Nature protocols*, vol. 1, no. 5, pp. 2305–2314, 2006.

[125] S. F. Parsons and E. D. Salmon, “Microtubule assembly in clarified Xenopus egg extracts.,” *Cell Motility and the Cytoskeleton*, vol. 36, no. 1, pp. 1–11, 1997.

[126] W. Thielicke and E. Stamhuis, “PIVlab – Towards User-friendly, Affordable and Accurate Digital Particle Image Velocimetry in MATLAB,” *Journal of Open Research Software*, vol. 2, Oct. 2014.